Homogenized limit analysis of FRP-reinforced masonry walls out-of-plane loaded

Journal Article

Author(s):
Milani, Gabriele

Publication date:
2009

Permanent link:
https://doi.org/10.3929/ethz-b-000115983

Rights / license:

Originally published in:
Computational Mechanics 43(5), https://doi.org/10.1007/s00466-008-0334-7

Comput Mech (2009) 43:617–639
DOI 10.1007/s00466-008-0334-7

ORIGINAL PAPER

Homogenized limit analysis of FRP-reinforced masonry walls out-of-plane loaded

Gabriele Milani

Received: 25 April 2008 / Accepted: 18 August 2008 / Published online: 9 September 2008

Abstract A three-dimensional (3D) homogenized limit analysis model for the determination of collapse loads of out-of-plane loaded FRP reinforced masonry walls is presented. Homogenization is performed on unreinforced masonry, whereas strips are applied at a structural level on the already homogenized material. Unreinforced masonry strength domain is obtained by means of a compatible approach in which bricks are supposed infinitely resistant and joints are reduced to interfaces with frictional-cohesive behavior and associated flow rule. A sub-class of elementary deformation modes is a-priori chosen in the representative volume element (RVE), mimicking typical failures due to joints cracking and crushing. Masonry strength domains are obtained equating power dissipated in the heterogeneous model with power dissipated in a fictitious homogeneous macroscopic plate. Afterwards, an upper bound FE limit analysis code is implemented to study entire unreinforced and FRP reinforced walls out-of-plane loaded. For unreinforced masonry, rigid infinitely resistant wedge-shaped 3D elements are used. The utilization of 3D elements is necessary to simulate the flexural strength increase induced by the introduction of FRP strips with negligible thickness, which are modeled by means of triangular rigid elements. FRP strips contribution is taken into account assuming that masonry and FRP layers interact by means of interfacial tangential actions. Internal power dissipation is possible at the interfaces between wedge adjoining elements (masonry failure), at the interfaces between triangular FRP and wedge masonry elements (delamination) and between triangular FRP adjoining elements (FRP failure). Two different structural examples are presented to validate the numerical model, namely a FRP reinforced masonry wall in cylindrical flexion and a set of masonry walls with openings in two-way bending. Results obtained with the model proposed fit well both experimental and numerical data available for all the cases analyzed, meaning that the procedure proposed can be used in building practice.

Keywords Masonry · FRP strips · Limit analysis · Out-of-plane loads

1 Introduction

Unreinforced masonry structures comprise a significant amount of the building stock in many countries worldwide, but their behavior under out-of-plane loads shows a low capacity to withstand to horizontal actions. Out-of-plane failures are mostly related to seismic and wind loads and the lack of out-of-plane strength is a primary cause of failure in different forms of masonry, particularly in the case of historical buildings (see for instance [1]). Consequently, many historical masonry structures require retrofitting to both comply with existing codes and improve out-of-plane strength.

Conventional retrofitting techniques, such as external reinforcement with steel plates, surface concrete coating and welded mesh, have proven to be impractical, time expensive and add considerable mass to the structure (which may increase earthquake-induced inertia forces). In this context, the utilization of “Fiber Reinforced Polymer” (FRP) strips as reinforcement instead of conventional methods is receiving growing attention in the scientific community, for the low invasiveness, durability and good performance at failure.

Despite the great importance and the increasing diffusion of such innovative strengthening technique, few numerical models devoted to the prediction of the ultimate load

G. Milani (✉)
Institute of Structural Engineering (IBK),
Swiss Federal Institute of Technology (ETHZ),
Wolfgang-Pauli-Strasse 15, Zürich, Switzerland
e-mail: milani@ibk.baug.ethz.ch

bearing capacity of FRP-reinforced masonry walls out-of-plane loaded [2,3] are nowadays at disposal.

In fact, numerical tools, to be reliable, should take into account several distinctive aspects related to both masonry and FRP reinforcement behavior at failure, such as masonry anisotropy [4,5], closely related to the constituent materials (mortar and units) and to the bond pattern, masonry limited compressive strength, and the fragile delamination of the FRP from the support [6], which depends on a number of concurring factors, among the others the most important being bricks strength (CNR-DT 200 [7]).

Furthermore, when dealing with out-of-plane actions, the role of vertical loads on both ductility and out-of-plane ultimate strength has not yet been sufficiently understood and brings additional complexity to the structural analyses.

Laboratory tests conducted in the past (see for instance [8,9] etc.) on brick masonry walls subjected to lateral loads, have shown both that failure takes place along a well-defined pattern of lines and that, in many cases, fractures occur at the interface between bricks and mortar. This suggests the utilization of the yield line theory to have a reliable prediction of both collapse loads and failure mechanisms without an excessive computational effort.

At present, the main problem in the development of accurate stress analyses for masonry structures is the definition and the use of suitable material constitutive laws. As a rule, three different approaches are possible, usually known as macro-modeling, micro-modeling and homogenization (see for instance [5,10–17]). While in micro-modeling (e.g. [16,17]) a separate discretization of bricks and mortar (usually reduced to interfaces) is assumed, macro-models [18,19] substitute the heterogeneous material with a fictitious anisotropic homogeneous one, thus needing much less time to be performed in complex non-linear analyses but requiring a calibration of the model with expensive experimental data fittings. Homogenization (e.g. [12,14,20]) may be regarded as a compromise between micro- and macro-modeling, since macroscopic masonry behavior is obtained solving suitable boundary values problems on the unit cell, thus taking into account constituent materials mechanical properties and geometry only at the micro-scale.

As well known, limit analysis (a valuable alternative to expensive non-linear FE simulations) has been widely used for the analysis at failure of masonry structures [12–14], because it requires only a reduced number of material parameters, providing limit multipliers of loads, failure mechanisms and, at least on critical sections, the stress distribution at collapse.

In this framework, with the aim of reproducing FRP-strengthened masonry panels behavior when loaded out-of-plane, a mesoscopic homogenization model is presented.

Masonry unreinforced strength domain is obtained by means of a compatible kinematic approach [10,21] in which joints are reduced to interfaces with a cohesive frictional behavior and bricks are supposed infinitely resistant. Subsequently, FRP strips are applied on the already homogenized material.

Masonry skeleton is represented by a three-dimensional (3D) discrete system of blocks interacting through interfaces (the mortar joints). Bricks are supposed infinitely resistant, whereas for joints a Mohr Coulomb failure criterion with tension cut-off and compressive limited strength is adopted.

A full description of the model can be given considering a representative volume constituted by a generic brick with its 6 neighbors. A sub-class of possible elementary deformation modes acting in the unit cell is a priori chosen in order to describe joints cracking under normal and tangential actions. Finally, power dissipated in the discrete model is equated to that dissipated in a continuum macroscopic 2D equivalent plate (identification). Since internal dissipation can take place only at the interface between bricks, a simple constrained minimization problem in few variables is obtained. Macroscopic masonry failure surfaces are numerically evaluated as a function of the macroscopic in-plane actions (shear and normal actions) and out-of-plane shear.

Macroscopic strength domains so obtained are then implemented in a novel upper bound FE limit analysis code for the analysis at collapse of entire FRP reinforced walls out-of-plane loaded. Rigid infinitely resistant wedge-shaped 3D elements are used to model masonry at structural level. The utilization of 3D elements is necessary to simulate the flexural strength increase obtained by the introduction of FRP strips with negligible thickness. On the other hand, wedge-shaped elements are utilized with the aim of reproducing possible diagonal failure occurring on masonry plates, due to the development of cracks (caused by bending and torsion) which zigzag between contiguous bricks.

FRP strips are modeled by means of triangular rigid elements. Masonry and FRP layers interact by means of interfacial tangential actions between triangles (FRP) and wedges (masonry). Furthermore, a possible limited tensile strength for the FRP reinforcement is considered at the interfaces between adjoining triangular elements. In this way, both delamination phenomenon at the FRP/masonry interface and FRP tensile failure may be taken into account. Despite the fact that delamination is a typical fragile phenomenon, an equivalent ultimate shear strength for FRP/masonry interface is assumed in the framework of limit analysis, following formulas provided by the recent Italian norm CNR-DT 200 [7] for the peak delamination strength. Furthermore, it has to be emphasized that the limit analysis approach here proposed is based on the use a perfectly-plastic material response for masonry and for the FRP/masonry interface, i.e. softening effect and limited ductility cannot be considered.

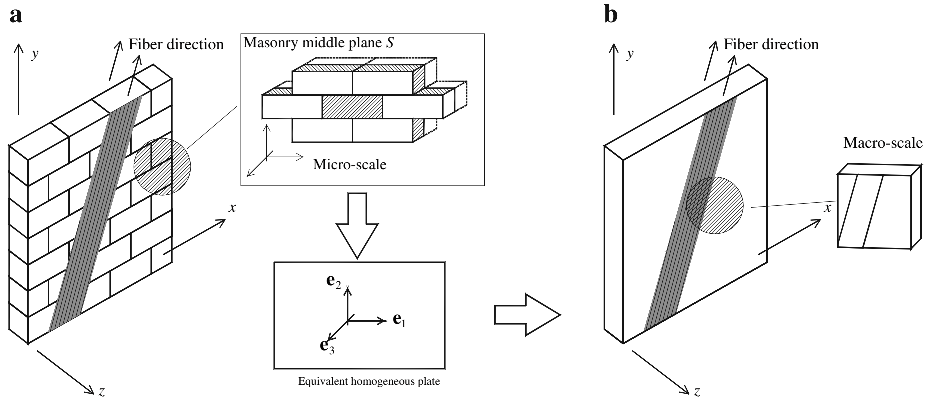

Reinforced masonry (heterogeneous)

Equivalent homogeneous continuous+ FRP

Fig. 1 Equivalent homogeneous model used for the analysis of FRP reinforced masonry. **a** micro-scale. **b** macro-scale

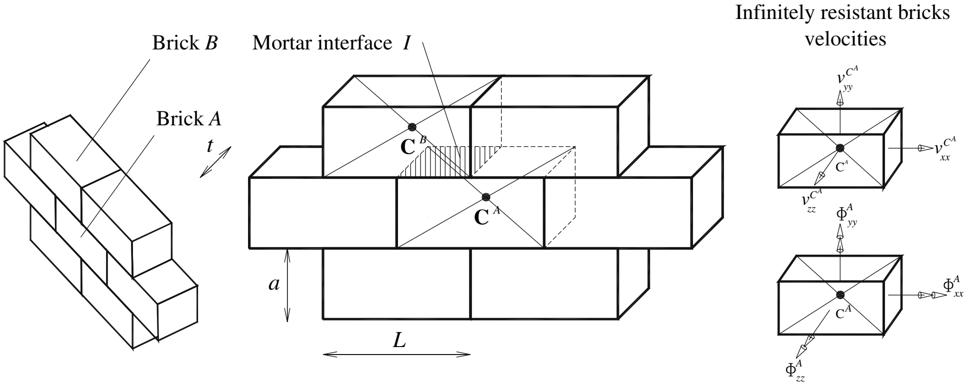

Fig. 2 Unreinforced masonry kinematic model. Two adjacent bricks (A, centroid $\mathbf{C}^A$ and B, centroid $\mathbf{C}^B$) connected by means of a mortar interface I where plastic dissipation occurs. For each brick three velocities unknowns and three rotation rates must be introduced in the optimization problem at a cell level (infinite strength of bricks hypothesis)

In order to validate the numerical model proposed, two different structural examples are analyzed, namely a FRP reinforced masonry wall in cylindrical flexion already studied experimentally and theoretically in [22] and a set of masonry walls with openings in two-way bending, experimentally tested by Chong et al. [23] in absence of FRP strengthening. Results obtained with the model proposed fit well both experimental (where available) and literature numerical data, meaning that the procedure proposed can be used by practitioners for an inexpensive evaluation of ultimate loads in presence of FRP strips.

2 The mesoscopic model

In what follows, the introduction of FRP strips on masonry surface (Fig. 1) is treated by means of a simplified *two steps* approach.

In the first step, here denoted as *micro-scale* (Fig. 1a), masonry is supposed unreinforced and homogenization is used to obtain brickwork macroscopic strength domain.

In the second step, denoted as *macro-scale* (Fig. 1b), FRP reinforcement strips are introduced on the already homogenized masonry material obtained from the first step and full FE structural analyses are performed on entire walls.

2.1 Micro-scale: unreinforced masonry

In the model, bricks are supposed infinitely resistant, whereas for joints a Mohr Coulomb failure criterion with tension cutoff and compressive limited strength is adopted. In this way, a full description of the model can be given at the *micro-scale* (see Fig. 2) considering a representative volume constituted by a generic brick interacting with its six neighbors. A subclass of possible elementary deformation modes acting in the unit cell is a priori chosen with the aim of describing joints cracking. Then, a numerical procedure of identification between the 3D discrete system and a continuum 2D equivalent model is proposed, equating internal dissipation of the two models.

The two-steps procedure presented results particularly efficient from a numerical point of view, permitting to analyze entire masonry walls without a distinct discretization of joints and bricks, thus (a) requiring a very limited number of optimization variables to be performed in comparison with standard heterogeneous approaches and (b) permitting in principle the analysis of entire retrofitted buildings.

Finally, it is worth noting that the homogenization approach proposed results somewhat different with respect to the original formulation presented in [10] for unreinforced masonry, because rigid 3D wedge elements are used at

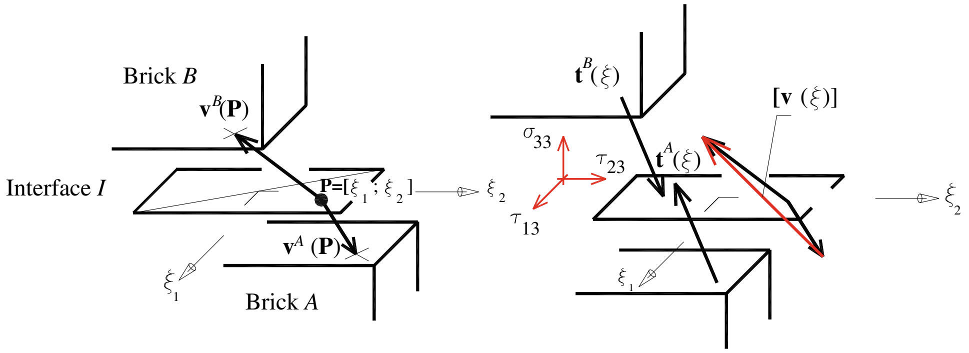

Fig. 3 Jump of velocities and stress field acting on an interface I between contiguous bricks A and B

a structural level for brickwork. Such a choice (a) requires to have at disposal only in-plane and shear homogenized masonry failure surfaces, thus limiting the computational effort both at a cell and structural level, (b) allows to well reproduce failures induced by inclined yield lines and (c) permits a simple evaluation (otherwise impossible) of the effective strengthening effect induced by a thin (highly resistant) strip placed at a distance equal to masonry semi-thickness with respect to brickwork middle plane.

2.1.1 *Heterogeneous model*

The motion of a generic brick A, see Fig. 2, is described as a function of its centroid (C^A) velocity $\mathbf{v}^{C^A}$ (components $v_{xx}^{C^A}$, $v_{yy}^{C^A}$ and $v_{zz}^{C^A}$) and of rotation rates vector $\mathbf{\Phi}^A$ (components Φ_{xx}^A, Φ_{yy}^A and Φ_{zz}^A).

When two contiguous bricks A and B are considered, the velocity of a generic point $\mathbf{P}$ in a position $\xi \in I$ belonging respectively to A and B (where I indicates the common interface between the two bricks, Fig. 3) is:

$$\begin{aligned}\mathbf{v}^A(\boldsymbol{\xi}) &= \mathbf{v}^{C^A} + \mathbf{M}(\mathbf{\Phi}^A)(\boldsymbol{\xi} - \mathbf{C}^A)\\ \mathbf{v}^B(\boldsymbol{\xi}) &= \mathbf{v}^{C^B} + \mathbf{M}(\mathbf{\Phi}^B)(\boldsymbol{\xi} - \mathbf{C}^B)\end{aligned} \tag{1}$$

where $\mathbf{M}(\mathbf{\Phi})$ is the following 3×3 skew matrix:

$$\mathbf{M}(\mathbf{\Phi}) = \begin{bmatrix} 0 & -\Phi_{zz} & \Phi_{yy} \\ \Phi_{zz} & 0 & -\Phi_{xx} \\ -\Phi_{yy} & \Phi_{xx} & 0 \end{bmatrix} \tag{2}$$

In Eq. (1) the position ξ of point $\mathbf{P}$ is evaluated referring to a local frame (ξ_1 ξ_2) with origin on the centroid on the interface, see Fig. 3. Jump of velocity $[\mathbf{v}(\boldsymbol{\xi})]$ between bricks A and B in a point $\boldsymbol{\xi} \in I$ is expressed by:

$$\begin{aligned}\lfloor \mathbf{v}(\boldsymbol{\xi}) \rfloor = \mathbf{v}^B(\boldsymbol{\xi}) - \mathbf{v}^A(\boldsymbol{\xi}) = \mathbf{v}^{C^A} - \mathbf{v}^{C^B}\\ + \mathbf{M}(\mathbf{\Phi}^A)(\boldsymbol{\xi} - \mathbf{C}^A) - \mathbf{M}(\mathbf{\Phi}^B)(\boldsymbol{\xi} - \mathbf{C}^B).\end{aligned} \tag{3}$$

Power dissipated at the interface I can be written as:

$$\begin{aligned}\pi &= \int_I \left[\mathbf{t}^A(\boldsymbol{\xi}) \cdot \mathbf{v}^A(\boldsymbol{\xi}) + \mathbf{t}^B(\boldsymbol{\xi}) \cdot \mathbf{v}^B(\boldsymbol{\xi})\right] dS\\ &= \int_I \mathbf{t}^A(\boldsymbol{\xi}) \cdot \left[\mathbf{v}(\boldsymbol{\xi})\right] dS\end{aligned} \tag{4}$$

where $\mathbf{t}^A(\boldsymbol{\xi}) = \left[\tau_{13}(\boldsymbol{\xi})\ \tau_{23}(\boldsymbol{\xi})\ \sigma_{33}(\boldsymbol{\xi})\right]^T$ ($\mathbf{t}^B(\boldsymbol{\xi})$) is the stress vector acting at $\boldsymbol{\xi}$ on brick $A(B)$, see Fig. 3, with $\mathbf{t}^A(\boldsymbol{\xi}) = -\mathbf{t}^B(\boldsymbol{\xi})$.

2.1.2 *Continuous model*

A standard 2D Cauchy continuum, identified by its middle plane S of normal $\mathbf{e}_3$ (Fig. 1), is assumed as plate homogenized model.

The velocity field of a point $\mathbf{P}$(coordinates $\left[x_1^P\ x_2^P\ x_3^P\right]$) belonging to the equivalent continuum plate is given by fields $\mathbf{w}(\mathbf{x})$ (components w_1, w_2 and w_3) and $\mathbf{\Psi}(\mathbf{x})$ (components Ψ_1 and Ψ_2), representing respectively the velocity and rotations rates of the plate in correspondence of the point $\mathbf{x} = \left[x_1^P\ x_2^P\ 0\right]$ laying in the middle plane of the plate.

Power dissipated by the equivalent plate model is:

$$\begin{aligned}\pi &= \left[N_{11}\ N_{12}\ N_{22}\right]\begin{bmatrix}\dot{E}_{11}\\ \dot{E}_{12}+\dot{E}_{21}\\ \dot{E}_{22}\end{bmatrix} + \left[T_{13}\ T_{23}\right]\begin{bmatrix}\dot{\gamma}_{13}\\ \dot{\gamma}_{23}\end{bmatrix}\\ &\quad + \left[M_{11}\ M_{12}\ M_{22}\right]\begin{bmatrix}\dot{\chi}_{11}\\ \dot{\chi}_{12}+\dot{\chi}_{21}\\ \dot{\chi}_{22}\end{bmatrix}\end{aligned} \tag{5}$$

where:

$$\begin{aligned}\dot{\mathbf{E}} &= \begin{bmatrix}\dot{E}_{11}\\ \dot{E}_{12}+\dot{E}_{21}\\ \dot{E}_{22}\end{bmatrix}\\ &= \frac{1}{t}\int_{-t/2}^{t/2}\begin{bmatrix}\partial w_1/\partial x_1 - x_3\partial\Psi_1/\partial x_1\\ \partial w_2/\partial x_1 + \partial w_1/\partial x_2 - x_3\left(\partial\Psi_1/\partial x_2 + \partial\Psi_2/\partial x_1\right)\\ \partial w_2/\partial x_2 - x_3\partial\Psi_2/\partial x_2\end{bmatrix} dx_3\end{aligned}$$

(in-plane strain rate vector, assuming with t masonry thickness);

$$\dot{\boldsymbol{\gamma}} = \begin{bmatrix} \dot{\gamma}_{13} \\ \dot{\gamma}_{23} \end{bmatrix} = \frac{1}{t} \int_{-t/2}^{t/2} \begin{bmatrix} \partial w_3/\partial x_1 + \partial w_1/\partial x_3 \\ \partial w_3/\partial x_2 + \partial w_2/\partial x_3 \end{bmatrix} dx_3$$

(shear strain rate);

$$\dot{\boldsymbol{\chi}} = \begin{bmatrix} \dot{\chi}_{11} \\ \dot{\chi}_{12} + \dot{\chi}_{21} \\ \dot{\chi}_{22} \end{bmatrix} = \frac{1}{t} \int_{-t/2}^{t/2} \begin{bmatrix} \partial \Psi_1/\partial x_1 \\ \partial \Psi_2/\partial x_1 + \partial \Psi_1/\partial x_2 \\ \partial \Psi_2/\partial x_2 \end{bmatrix} dx_3$$

(strain rate vector);

$\mathbf{M} = \begin{bmatrix} M_{11} & M_{12} & M_{22} \end{bmatrix}^T$, with M_{11} and M_{22} indicating bending and M_{12} torsion;

$\mathbf{T} = \begin{bmatrix} T_{13} & T_{23} \end{bmatrix}^T$;

$\mathbf{N} = \begin{bmatrix} N_{11} & N_{12} & N_{22} \end{bmatrix}^T$.

$$\dot{\mathbf{E}} = \begin{bmatrix} \dot{E}_{11} \\ \dot{E}_{12} + \dot{E}_{21} \\ \dot{E}_{22} \end{bmatrix} = \frac{1}{t} \int_{-t/2}^{t/2} \begin{bmatrix} \partial w_1/\partial x_1 - x_3 \partial \Psi_1/\partial x_1 \\ \partial w_2/\partial x_1 + \partial w_1/\partial x_2 \\ \quad -x_3 \left(\partial \Psi_1/\partial x_2 + \partial \Psi_2/\partial x_1\right) \\ \partial w_2/\partial x_2 - x_3 \partial \Psi_2/\partial x_2 \end{bmatrix} dx_3$$

$$\dot{\boldsymbol{\gamma}} = \begin{bmatrix} \dot{\gamma}_{13} \\ \dot{\gamma}_{23} \end{bmatrix} = \frac{1}{t} \int_{-t/2}^{t/2} \begin{bmatrix} \partial w_3/\partial x_1 + \partial w_1/\partial x_3 \\ \partial w_3/\partial x_2 + \partial w_2/\partial x_3 \end{bmatrix} dx_3$$

$$\dot{\boldsymbol{\chi}} = \begin{bmatrix} \dot{\chi}_{11} \\ \dot{\chi}_{12} + \dot{\chi}_{21} \\ \dot{\chi}_{22} \end{bmatrix} = \frac{1}{t} \int_{-t/2}^{t/2} \begin{bmatrix} \partial \Psi_1/\partial x_1 \\ \partial \Psi_2/\partial x_1 + \partial \Psi_1/\partial x_2 \\ \partial \Psi_2/\partial x_2 \end{bmatrix} dx_3 \tag{6}$$

2.1.3 Simplified homogenization

In order to substitute the heterogeneous material with the homogeneous equivalent 2D model, a simple compatible identification model is proposed, assuming that power dissipated by blocks [Eq. (4)] equates power dissipated by the equivalent model, Eq. (5).

At this aim, fields $\mathbf{w}(\mathbf{x})$ and $\boldsymbol{\Psi}(\mathbf{x})$ are a priori chosen as a combination of elementary deformations in the unit cell, corresponding to actual failure mechanisms occurring, according to experimental evidences, in presence of running bond brickwork with weak joints reduced to interfaces. From a practical point of view, fields $\mathbf{w}(\mathbf{x})$ and $\boldsymbol{\Psi}(\mathbf{x})$ corresponding to each sub-class of regular motions are obtained assuming alternatively one component of vector $\dot{\mathbf{E}}$, $\dot{\boldsymbol{\gamma}}$ or $\dot{\boldsymbol{\chi}}$ unitary and setting all the other components equal to zero, subsequently choosing the most simple polynomial expressions for $\mathbf{w}(\mathbf{x})$ and $\boldsymbol{\Psi}(\mathbf{x})$ which comply Eq. (6). Once that fields $\mathbf{w}(\mathbf{x})$ and $\boldsymbol{\Psi}(\mathbf{x})$ are known from the procedure described, rotations rates and velocities of each bricks belonging to the REV in the heterogeneous model are determined assuming as point $\mathbf{x}$ the centroid of the brick under consideration.

For instance, when only $\dot{\chi}_{11} \neq 0$ is applied on the REV, a choice for $\mathbf{w}(\mathbf{x})$ and $\boldsymbol{\Psi}(\mathbf{x})$ fields is:

$$\begin{aligned} \Psi_1 &= \dot{\chi}_{11} x_1 \\ w_1 &= \dot{\chi}_{11} x_1 x_3 \\ w_2 &= 0 \\ w_3 &= -\dot{\chi}_{11} x_1^2/2 \end{aligned} \tag{7}$$

Equation (7) allows to directly determine velocities and rotations of each block, provided that coordinated of the respective centroid are introduced in Eq. (7).

Since the aim of this paper is to model the strengthening effect induced by FRP in bending, at the macro-scale homogenized three-dimensional wedge-shaped elements are used for masonry (see following sections). Consequently, unreinforced brickwork behavior in flexion is obtained by integration of in plane actions at a structural level (step two).

Therefore, at the micro-scale, it is possible to limit the study to in-plane and out-of-plane shear actions ($\dot{\mathbf{E}}$ and $\dot{\boldsymbol{\gamma}}$ respectively). The error introduced by this simplified approach is negligible in almost all the cases of technical interest, since it is well known that only tensile regime is active in bending, i.e. only 2 plastic multipliers on the thickness are needed. Figure 4a–c shows the effect on the elementary cell of homogeneous in-plane deformations $\dot{\mathbf{E}}$ (respectively stretching along horizontal axis, vertical axis and shear).

Finally, Fig. 5 refers to the application of $\dot{\boldsymbol{\gamma}}$ out-of-plane shear deformation rate. In particular, Fig. 5a shows the $\dot{\gamma}_{13}$ component, while Fig. 5b shows the $\dot{\gamma}_{23}$ component. It is particularly evident that, when a $\dot{\gamma}_{13} \neq 0$ is applied, both head and bed joints contribute to the internal power dissipation.

2.1.4 Unreinforced masonry failure surfaces

In this section, following the original formulation by Suquet [24], a general numerical procedure for obtaining macroscopic in- and out-of-plane unreinforced masonry failure surfaces is presented.

One of the basic assumptions of this approach is the utilization of associated flow rules for the constituent materials. Nevertheless, it is worth mentioning that sliding occurs in mortar joints with almost zero dilatancy, with typical non-associativity. The violation of one of the hypotheses of classic limit analysis ([25,26] etc.), implies that the uniqueness of the ultimate load may be lost and a multiplicity of solutions can exist for limit analysis problems, see Begg and Fishwick [27].

On the contrary, the assumption of associated flow rules assure the uniqueness of the ultimate load factor and lead to

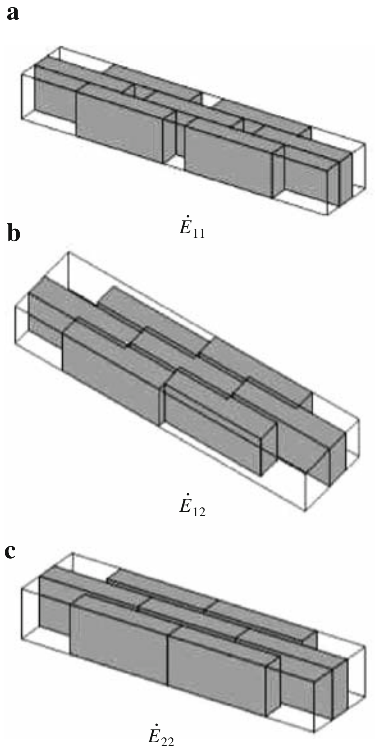

Fig. 4 Elementary in plane homogeneous deformations applied to the representative volume element. **a** $\dot{E}_{11}$. **b** $\dot{E}_{12}$. **c** $\dot{E}_{22}$

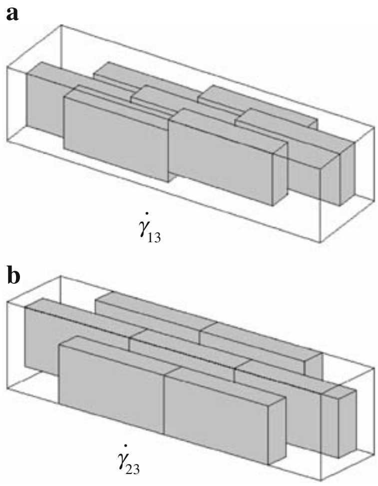

Fig. 5 Elementary homogeneous shear deformations applied to the representative volume element. **a** $\dot{\gamma}_{13}$. **b** $\dot{\gamma}_{23}$

simple optimization problems which can be handled easily with LP packages. In any case, it has been demonstrated that associated limit analysis gives reliable results when failure mechanisms are mainly due to joints tensile cracking (see for instance [8,10,19]). As well known, out-of-plane masonry failure occurs almost only with joints tensile regime active, therefore associated limit analysis seems particularly suited for numerical analyses at failure.

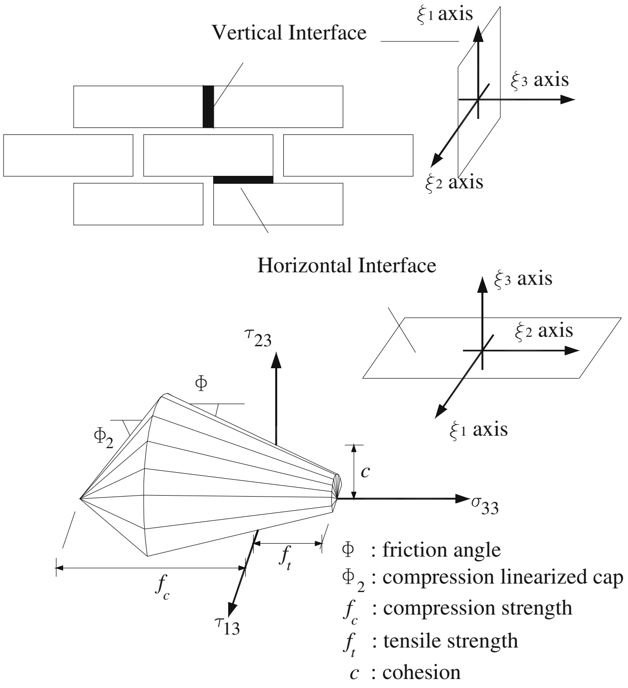

Fig. 6 Piecewise linear approximation of the failure criterion adopted for joints. Mohr-Coulomb failure criterion with tension cut-off and linearized compression cap

Any non-linear failure criterion $\phi = \phi(\boldsymbol{\sigma})$ for joints can be assumed for the model at hand. In any case, basic failure modes for masonry walls with weak mortar are a mixing of sliding along the joints (a), direct tensile splitting of the joints (b) and compressive crushing at the interface between mortar and bricks (c). These modes can be well reproduced adopting a Mohr-Coulomb failure criterion combined with tension cut-off and cap in compression, see Fig. 6, as suggested by Lourenço and Rots [17].

Aiming at treating the problem in the framework of linear programming, within each interface I of area A^I, a piecewise linear approximation of the failure surface $\phi = \phi(\boldsymbol{\sigma})$ is adopted, constituted by n_{lin} planes of equation $\mathbf{A}_i^{IT}\boldsymbol{\sigma} = c_i^I$ $1 \leq i \leq n_{lin}$, where $\boldsymbol{\sigma} = [\sigma_{33}\ \tau_{13}\ \tau_{23}]$, σ_{33} is the normal stress on the interface and τ_{13} and τ_{23} are tangential stresses along two assigned perpendicular directions ($A_i^{1I}\sigma_{33} + A_i^{2I}\tau_{13} + A_i^{3I}\tau_{23} = c_i^I$ is the ith linearization plane of the interface I, with $\mathbf{A}_i^{IT} = \left[A_i^{1I}\ A_i^{2I}\ A_i^{3I}\right]$), Figs. 3 and 6.

Jump of velocity on interfaces varies linearly in the discrete model, Eq. (3). Thus, for each interface, only $3 \times n_{lin}$ independent plastic multiplier rates have to be introduced as optimization variables.

Furthermore, for each interface I between contiguous bricks, the following equality constraints between plastic multiplier rates $\dot{\lambda}_i^I(\xi_1, \xi_2)$ and jump of velocity $[\mathbf{v}(\xi_1, \xi_2)]$ on the interface must be imposed:

$$[\mathbf{v}(\xi_1, \xi_2)] = \sum_{i=1}^{n_{lin}} \dot{\lambda}_i^I(\xi_1, \xi_2)\frac{\partial \phi}{\partial \boldsymbol{\sigma}} \tag{8}$$

where:

- $\xi = (\xi_1, \xi_2)$ is a local frame of reference laying on the interface plane and with axis ξ_3 orthogonal to the interface plane, Figs. 3 and 6;
- $[\mathbf{v}(\xi_1, \xi_2)] = \left[\,\Delta v_{33}\ \Delta v_{13}\ \Delta v_{23}\,\right]^T$ is the jump of velocity field (linear in (ξ_1, ξ_2)) on the I-th interface and Δv_{ij} corresponds to the jump along the direction j.
- $\dot{\lambda}_i^I(\xi_1, \xi_2)$ is the i-th plastic multiplier rate field (linear in (ξ_1, ξ_2)) of the interface I, associated to the i-th linearization plane of the failure surface.

It is worth noting that, in order to satisfy Eq. (8) for each point of the interface I, nine equality constraints for each interface have to be imposed, that corresponds to evaluate (8) in three different positions $P_k = (\xi_1^{P_k}, \xi_2^{P_k})$ on the interface I as follows:

$$\left[\mathbf{v}\left(\xi_1^{P_k}, \xi_2^{P_k}\right)\right] = \sum_{i=1}^{n_{lin}} \dot{\lambda}_i^I\left(\xi_1^{P_k}, \xi_2^{P_k}\right)\frac{\partial \phi}{\partial \boldsymbol{\sigma}} \quad k = 1, 2, 3 \tag{9}$$

where $\dot{\lambda}_i^I(\xi_1^{P_k}, \xi_2^{P_k})$ is the is i-th plastic multiplier rate of the interface I corresponding to $P_k = (\xi_1^{P_k}, \xi_2^{P_k})$.

From previous equations, internal power dissipated on the I-th interface can be written as:

$$\begin{aligned}\pi_{\text{int}}^I &= \int_{A^I} [\mathbf{v}]^T \boldsymbol{\sigma}\, dA^I = \int_{A^I} \sum_{i=1}^{n_{lin}} \dot{\lambda}_i^I(\xi_1, \xi_2)\left[\frac{\partial \phi}{\partial \boldsymbol{\sigma}}\right]^T \boldsymbol{\sigma}\, dA^I \\ &= \frac{1}{4}\sum_{i=1}^{n_{lin}} c_i^I \sum_{k=1}^{4} \dot{\lambda}_i^I\left(\xi_1^{P_k}, \xi_2^{P_k}\right) A^I\end{aligned} \tag{10}$$

where $k = 4$ depends linearly on $k = 1, 2, 3$.

External power dissipated can be written as $\pi_{\text{ext}} = \left(\boldsymbol{\Sigma}_0^T + \lambda \boldsymbol{\Sigma}_1^T\right)\mathbf{D}$, where $\boldsymbol{\Sigma}_0$ is the vector of permanent loads, λ is the load multiplier, $\boldsymbol{\Sigma}_1^T$ is the unitary vector of loads dependent on the load multiplier (i.e. the optimization direction in the space of macroscopic stresses) and $\mathbf{D}$ is the vector of macroscopic kinematic descriptors. $\mathbf{D}$ collects in-plane deformation rates ($\dot{E}_{11}\ \dot{E}_{12}\ \dot{E}_{22}$) and shear deformation rates ($\dot{\gamma}_{13}\ \dot{\gamma}_{23}$).

As the amplitude of the failure mechanism is arbitrary, a further normalization condition $\boldsymbol{\Sigma}_1^T\mathbf{D} = 1$ is usually introduced. Hence, the external power becomes linear in $\mathbf{D}$ and λ and can be written as follows $\pi_{\text{ext}} = \boldsymbol{\Sigma}_0^T\mathbf{D} + \lambda$.

From Eqs. (3) and (7), a further set of linear equality constraints has to be imposed at each interface I, involving vector $\mathbf{D}$ and jump of displacements field $[\mathbf{v}(\xi_1, \xi_2)]$:

$$[\mathbf{v}(\xi_1, \xi_2)] = \mathbf{G}^I(\xi_1, \xi_2)\,\mathbf{D} \tag{11}$$

where $\mathbf{G}^I(\xi_1, \xi_2)$ is a 3×5 matrix which depends only on the geometry of the interface under consideration (see Fig. 6).

From Eqs. (9)–(11) and from the kinematic formulation of limit analysis, the following constrained minimization problem has to be solved to obtain masonry failure surfaces:

$$\begin{cases}\lambda = \min\limits_{\hat{\mathbf{x}}=[\mathbf{D},\lambda_i^I(P_k)]} \sum_{I=1}^{n^I} \pi_{\int}^I - \Sigma_0^T\mathbf{D} \\ \Sigma_1^T\mathbf{D} = 1 \\ \mathbf{G}^I(P_k)\mathbf{D} = [\mathbf{v}(P_k)] = \sum_{i=1}^{n_{lin}} \dot{\lambda}_i^I\left(\xi_1^{P_k}, \xi_2^{P_k}\right)\frac{\partial \phi}{\partial \boldsymbol{\sigma}} \quad P_k \in I\end{cases} \tag{12}$$

where n^I is the total number of interfaces considered and $\hat{\mathbf{x}}$ is the vector of total optimization unknowns. Linear programming problem (12) involves a relatively small number of optimization variables and therefore can be solved both by means of simplex and interior point methods (vector $\hat{\mathbf{x}}$ of global unknowns collects only $3 \cdot n_{lin} \cdot n^I$ plastic multiplier rates and 5 macroscopic kinematic variables $\mathbf{D}$). When it is required to investigate also masonry homogenized flexural behavior, $\mathbf{D}$ is a vector of length 8 with $\hat{\Phi} = \hat{\Phi}(N_{11}, N_{12}, N_{22}, M_{11}, M_{12}, M_{22}, T_{13}, T_{23})$.

Obviously, optimal value λ obtained from Eq. (12) represents only a point on $\hat{\Phi}$, i.e. the intersection between surface $\hat{\Phi}$ and the direction unit vector $\boldsymbol{\Sigma}_1$ in the eight-dimensional space $\Sigma = (N_{11}, N_{12}, N_{22}, M_{11}, M_{12}, M_{22}, T_{13}, T_{23})$. Consequently, in order to obtain a reliable linear approximation of $\hat{\Phi}$ by means of Delaunay tessellations, linear programming problem (12) has to be solved several times, each problem corresponding to a different $\boldsymbol{\Sigma}_1$ direction.

As already discussed, for the problem at hand, out-of-plane masonry behavior under M_{11}, M_{22} and M_{12} actions is modeled only at a structural level by integration of in-plane actions. Therefore, here only $\hat{\Phi} = \hat{\Phi}(N_{11}, N_{12}, N_{22}, T_{13}, T_{23})$ masonry strength domain projections in the space of membrane and out-of-plane shear actions are considered.

2.1.5 A meaningful application at a cell level

The masonry material considered by Chong et al. [23] for the experimental evaluation of collapse loads of walls in two-way bending is here analyzed. The same example will be also analyzed at a structural level in the following section. Bricks with dimensions 215 × 65 × 102.5 mm^3 with joint thickness equal to 10 mm were used in the experimentation. Mechanical properties at failure adopted for the constituent materials are summarized in Table 1. For mortar joints, a linerized Lourenço and Rots [17] failure criterion is adopted, whereas bricks are assumed infinitely resistant.

Masonry mechanical properties at failure in flexion were measured by Chong et al. [23] through experimentation on several wallettes out-of-plane loaded. Experimental values for vertical f_{tx} and horizontal f_{ty} flexural strengths were 2.28 and 0.97 N/mm^2 respectively.

Table 1 Chong et al. [23] experimental tests

Mortar joints mechanical properties		
f_t	0.32	MPa
c	f_t	MPa
Φ	36°	–
Φ_2	45°	–
f_c	8	MPa

Mechanical properties assumed for mortar joints reduced to interfaces (a linearized Lourenço and Rots failure criterion is used; f_t is mortar tensile strength; c is mortar cohesion, Φ is the friction angle, Φ_2 is the angle of the linearized compressive cap and f_c is mortar compressive strength). Mortar joints reduced to interfaces with linearized Lourenço-Rots failure criterion

Table 1 numerical values do not correspond to Chong et al. [23] data, due to the fact that f_{tx} and f_{ty} are indirect quantities obtained from experimental collapse moments M, assuming a linear elastic stress distribution along the thickness t of the wall (i.e. $M = f_t t^2/6$). Contrarily to Chong et al. [23] elastic assumption, Table 1 values for f_t correspond to an elastic-plastic stress distribution along the thickness (see [13]), hence they are equal to Chong et al. [23] data divided by three.

In Fig. 7, $N_h - N_v$ masonry in-plane strength domains recovered with the model proposed are reported for three different orientations of bed joint with respect to horizontal homogenized membrane action N_h (N_v in Fig. 7 represents vertical homogenized membrane action).

Results show that the model is capable of reproducing the typical anisotropic behavior of masonry along the material axes. Since a reliable evaluation of masonry ultimate strength is crucial at a structural level (especially when inclined yield lines with respect to bed joint orientation are considered), the model proposed seems particularly suited for a fast and accurate analysis at collapse of brickwork panels in flexure.

2.2 Structural level: collapse loads evaluation by means of an upper bound approach

A 3D FE kinematic limit analysis model for masonry walls reinforced with FRP strips and subjected to combined in- and out-of-plane actions is presented in this section.

The introduction of FRP strips is treated in what follows making use of the mesoscopic model previously presented.

A reinforced masonry wall Ω strengthened with FRP strips of width $l_w^{(k)}$, length $l_s^{(k)}$ and direction $\vartheta^{(k)}$, see Fig. 8, is considered. We indicate with Ω_f the reinforced part of the wall, with (k) the kth strip and with Ω_m the unreinforced part of $\Omega\,(\Omega_f \cup \Omega_m = \Omega)$. Unitary vectors $\mathbf{s}^{(k)}$, $\mathbf{r}^{(k)}$ and $\mathbf{t}^{(k)}$ represent respectively the directions parallel and orthogonal to the $\vartheta^{(k)}$ direction of the kth strip ($\mathbf{r}^{(k)}$ belongs to strips plane). As already discussed, Ω_m is discretized with rigid wedges with possible jump of velocities at the interfaces, whereas masonry is substituted with a homogeneous fictitious material obtained from homogenization [Eq. (12)]. Ω_f is modeled by means of a combination of wedges (masonry) and triangles (FRP), mutually interacting by means of normal and tangential stresses at the common interface, Figs. 8 and 9. Discretization is obtained automatically by means of a commercial preprocessor (namely Strand 7.2 [28]).

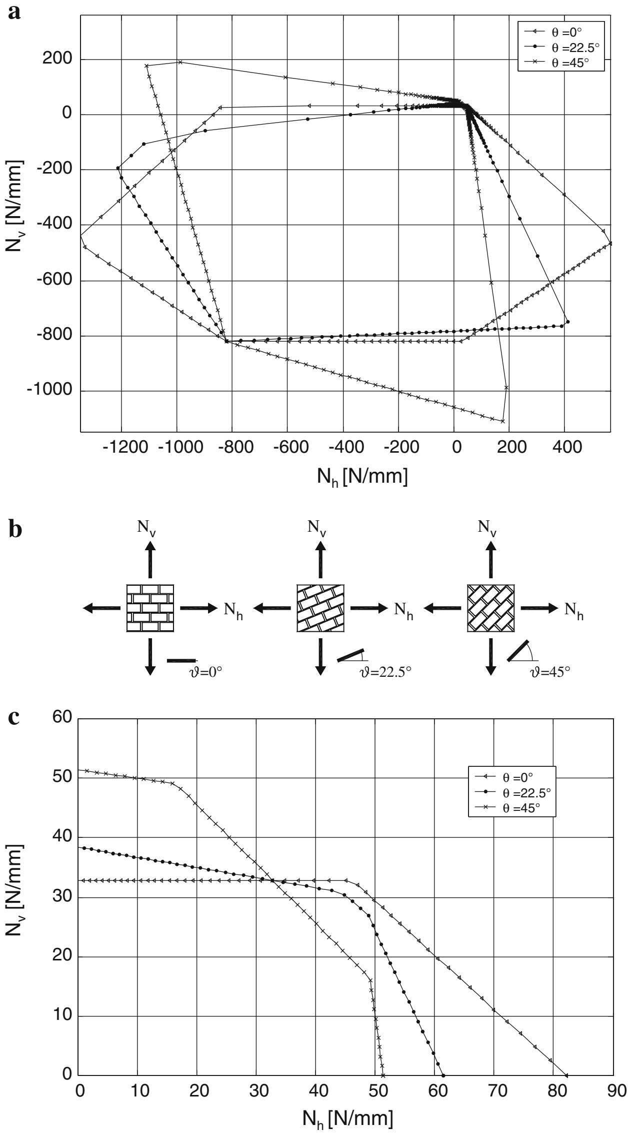

Fig. 7 Chong et al. masonry in-plane failure surfaces **(a)** at different angles between N_h and mortar joint direction **(b)** and detail of the tensile region **(c)**

2.2.1 Masonry elements (wedges)

A six-noded rigid masonry wedge, Fig. 9, is considered. For each element, three centroid velocity unknowns u_{xx}^{M},

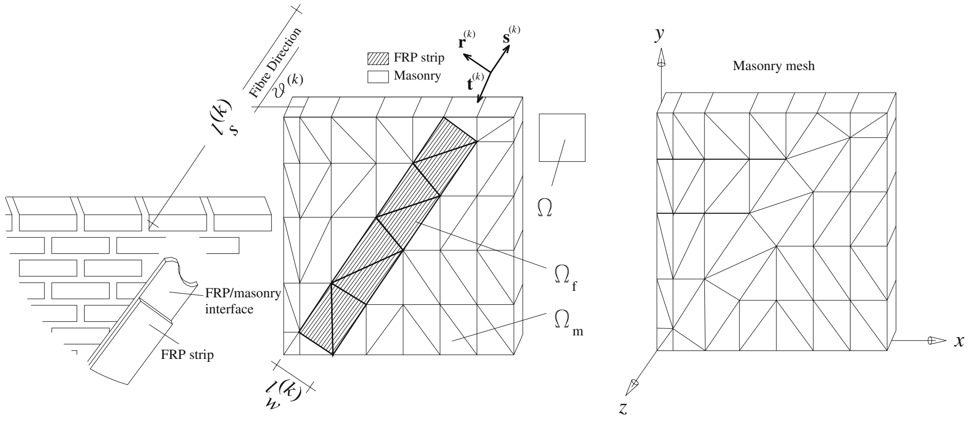

Fig. 8 Geometry of a generic reinforced masonry wall, FE discretization by means of wedges (masonry) and triangular elements (FRP) and geometrical properties of FRP strips

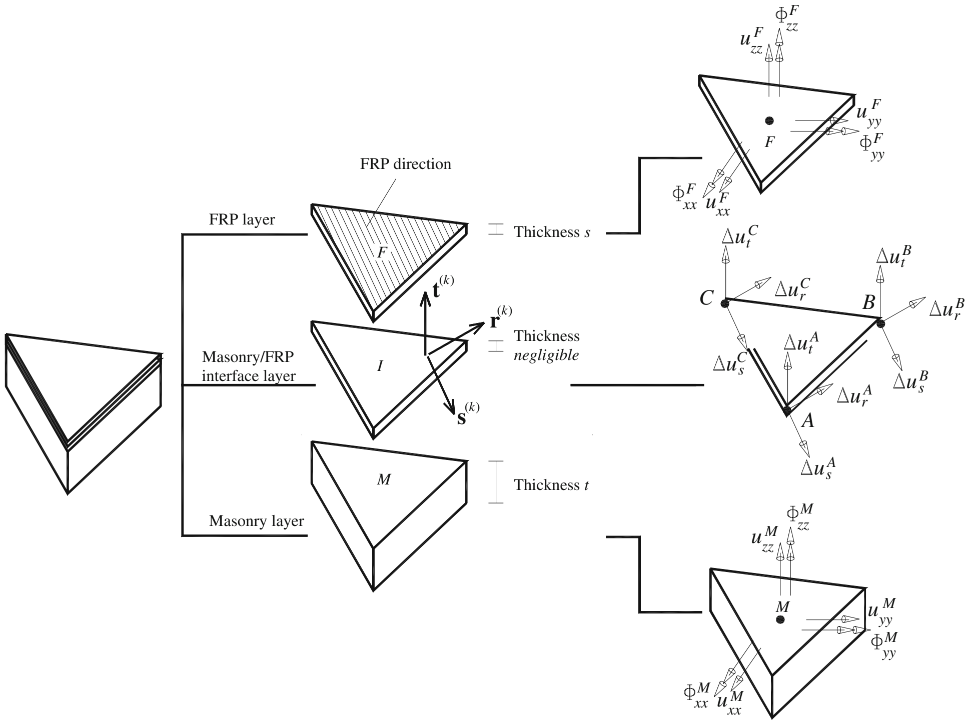

Fig. 9 Multi-layer approach for masonry reinforced with FRP (Ω_f) and kinematic variables involved. FRP is modeled by means of infinitely resistant triangular elements, whereas masonry is modeled with infinitely resistant wedges. A possible jump of displacement can occur at the FRP/masonry interface (delamination)

u_{yy}^M *and* u_{zz}^M (two horizontal and one vertical velocity collected in the vector $\mathbf{u}^M = \left[u_{xx}^M \; u_{yy}^M \; u_{zz}^M \right]^T$) and three rotation rates Φ_{xx}^M, Φ_{yy}^M and Φ_{zz}^M (corresponding to rotation rates along coordinate axes and collected in the vector $\mathbf{\Phi}^M = \left[\Phi_{xx}^M \; \Phi_{yy}^M \; \Phi_{zz}^M \right]^T$) are necessary to completely describe velocity field inside the element.

Differently from a well known elastic FE discretization, several nodes may share the same coordinate, being each node associated with only one element. In this way, at each interface between adjacent wedges, possible jumps of velocities can occur. Since velocities interpolation inside each wedge is linear, jumps of velocities field on interfaces vary linearly. Hence, for each interface, nine unknowns (three per node) are introduced and collected in the following vector:

$$\Delta\mathbf{u}^I = \left[\Delta u^1 \; \Delta v_1^1 \; \Delta v_2^1 \; \Delta u^2 \; \Delta v_1^2 \; \Delta v_2^2 \; \Delta u^3 \; \Delta v_1^3 \; \Delta v_2^3 \right]^T \tag{13}$$

representing the normal (Δu^i) and tangential ($\Delta v_1^i \; \Delta v_2^i$) jumps of velocities (with respect to a suitable local interface frame of reference) calculated on nodes 1, 2 and 3 of the interface (Fig. 10). Obviously, being velocity interpolation linear on the interface, node 4 jump of velocities (Δu^4, Δv_1^4 and Δv_2^4) turns out to be linearly dependent on $\Delta\mathbf{u}^I$.

With reference to Fig. 10, we choose a local interface frame of reference with axis x_1^I connecting nodes 1 and 2, x_2^I

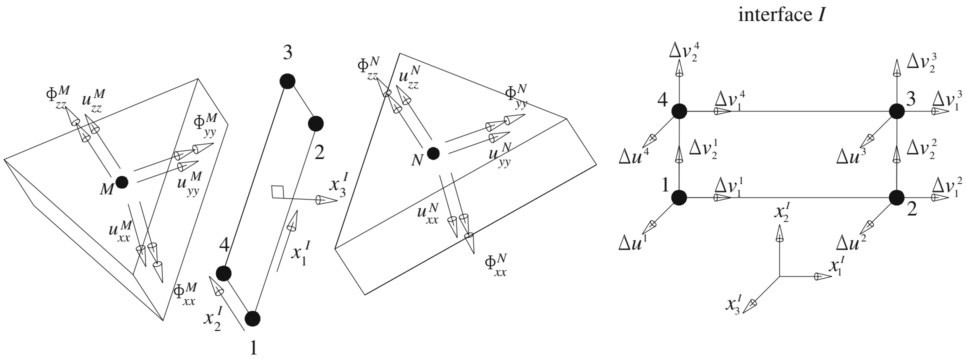

Fig. 10 Jump of velocities field in correspondence of a masonry interface between contiguous wedge-shaped elements

lying on the interface plane but perpendicular to x_1^I and x_3^I perpendicular to the interface.

Hence, for any pair of nodes of the interface belonging to elements $M-N$, the tangential and normal velocity jumps can be written in terms of the Cartesian nodal velocities of $M-N$ as:

$$\begin{aligned}\Delta v_1^f &= r_{11}\left(u_{xx}^{Mp}-u_{xx}^{Ns}\right)+r_{12}\left(u_{yy}^{Mp}-u_{yy}^{Ns}\right)\\&\quad+r_{13}\left(u_{zz}^{Mp}-u_{zz}^{Ns}\right)\\\Delta v_2^f &= r_{21}\left(u_{xx}^{Mp}-u_{xx}^{Ns}\right)+r_{22}\left(u_{yy}^{Mp}-u_{yy}^{Ns}\right)\\&\quad+r_{23}\left(u_{zz}^{Mp}-u_{zz}^{Ns}\right)\\\Delta u^f &= r_{31}\left(u_{xx}^{Mp}-u_{xx}^{Ns}\right)+r_{32}\left(u_{yy}^{Mp}-u_{yy}^{Ns}\right)\\&\quad+r_{33}\left(u_{zz}^{Mp}-u_{zz}^{Ns}\right)\end{aligned}\tag{14}$$

where

- $f=1,2,3$ indicates the interface node;
- $r_{ij}=(\Delta\mathbf{v}_i/\|\Delta\mathbf{v}_i\|)^T\mathbf{e}_j$; $(\Delta\mathbf{v}_i/\|\Delta\mathbf{v}_i\|)$ is the versor of the ith axis of the local frame of reference, whereas $\mathbf{e}_j$ indicates the versor of the jth axis of the local frame of reference.

After elementary assemblage operations on (14), it is possible to show that, for each interface, the following equations can be written:

$$\mathbf{A}_{11}^{eq}\mathbf{u}^{Mp}+\mathbf{A}_{12}^{eq}\mathbf{u}^{Ns}+\mathbf{I}_{13}^{eq}\Delta\mathbf{u}^I=\mathbf{0}\tag{15}$$

where $\mathbf{u}^{Mp}$ and $\mathbf{u}^{Ns}$ are the 6×1 vectors that collect velocities of elements M and N respectively, $\mathbf{A}_{11}^{eq}$, $\mathbf{A}_{12}^{eq}$ and $\mathbf{I}_{13}^{eq}$ are 9×6, 9×6 and 9×9 (identity) matrices respectively (depending only on the geometry of the interface).

It is worth noting that, to be kinematically admissible, ad thus provide an upper bound of the collapse load, the velocity field must satisfy the set of constraints imposed by an associated flow rule at each interface. In order to evaluate power dissipation π^M on masonry interfaces, for each interface I a linearization of masonry strength domain with N_I^{pl} planes (in the form $\sigma_{nn}A_{nn-i}^I+\tau_{1t}A_{1t-i}^I+\tau_{2t}A_{2t-i}^I=B_i^I$ $i=1,\ldots,N_I^{pl}$) is provided. Such a linearization for each interface (and, in principle, for each point of the interface) can be obtained from the homogenization technique described in the previously section and exploiting the procedure recommended by Krabbenhoft et al. [29] to obtain interfaces strength domains from the corresponding failure surfaces in continuum. σ_{nn}, τ_{1t} and τ_{2t} represent the stress components acting perpendicularly to the interface plane (σ_{nn}), along $x_1^I(\tau_{1t})$ and $x_2^I(\tau_{2t})$.

Being jump of velocities linear on masonry interfaces, plastic flow constraints only on three vertices f of the rectangular interface must be imposed:

$$\Delta u^f=\sum_{i=1}^{N_I^{pl}}\dot{\lambda}_i^{I,f}A_{nn-i}^I\quad\Delta v_1^f=\sum_{i=1}^{N_I^{pl}}\dot{\lambda}_i^{I,f}A_{1t-i}^I$$
$$\Delta v_2^f=\sum_{i=1}^{N_I^{pl}}\dot{\lambda}_i^{I,f}A_{2t-i}^I f\tag{16}$$

where:

- $f=1,2,3$;
- Δu^f represents the jump of displacements normal to the interface;
- Δv_1^f and Δv_2^f are jumps of displacement along perpendicular axes 1 and 2 on the interface plane, see Fig. 10;
- $\dot{\lambda}_i^{I,f}$ is the plastic multiplier rate of the ith linearization plane (vertex f, interface I).

From Eq. (16), within each interface I of area A^M, the power dissipated is:

$$\pi^M=\frac{A^M}{4}\sum_{f=1}^{4}\sum_{i=1}^{N_I^{pl}}\dot{\lambda}_i^{I,f}B_i^I\tag{17}$$

where index $f=4$ is a linear combination of previous indices.

Further equality constraints must be imposed on masonry elements, corresponding to boundary conditions on velocities (representing external constraints). Boundary conditions are imposed in a similar way with respect to classic

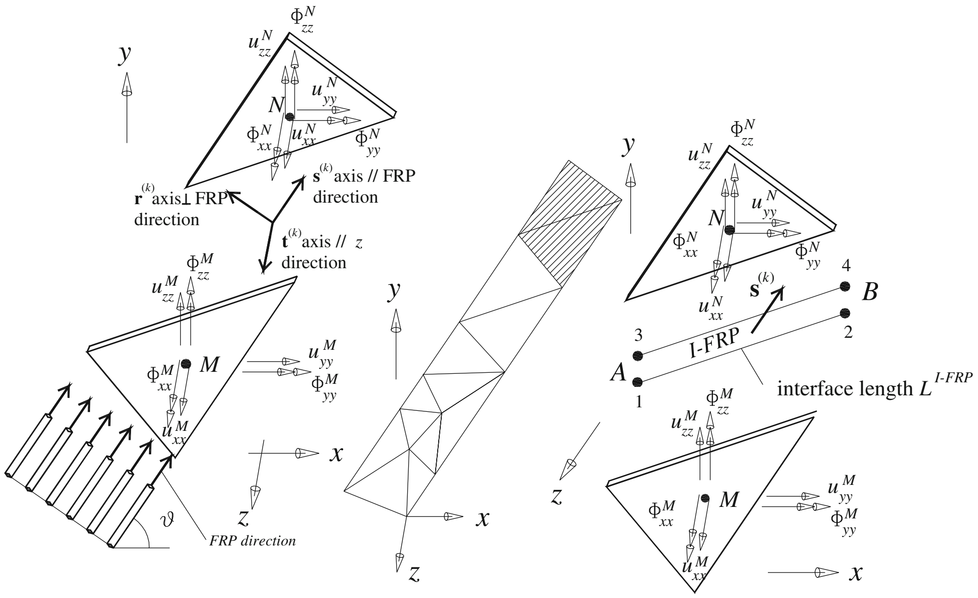

Fig. 11 Possible jump of displacements along FRP direction occurring at the interface between two FRP contiguous triangles

elastic finite elements. As a rule, for an element B to which prescribed velocities $\bar{\mathbf{u}}$ are assumed on some vertices, the following equality constraints are imposed:

$$\mathbf{A}^{eq}_{21}\begin{bmatrix}\mathbf{u}^B\\ \Phi^B\end{bmatrix} = \bar{\mathbf{u}} \tag{18}$$

where $\mathbf{A}^{eq}_{21}$ is a $m \times 6$ matrix of coefficients and all the other symbols have been already introduced.

2.2.2 FRP elements (triangles)

Triangular rigid and infinitely resistant elements are used to model FRP strips. Plastic dissipation is allowed only at the interfaces between contiguous elements due to stresses acting on the fibers direction (Fig. 11). Therefore, continuity of the velocity field is imposed at each interface between contiguous FRP triangular elements only along directions $\mathbf{r}^{(k)}$ and $\mathbf{t}^{(k)}$ (see Fig. 11) whereas a possible jump of velocities is supposed to occur along direction $\mathbf{s}^{(k)}$.

Let two contiguous FRP elements M and N be considered, see Fig. 11. Their centroid velocities and rotation rates are $\mathbf{u}^M = \left[u^M_{xx}\ u^M_{yy}\ u^M_{zz}\right]^T$, $\mathbf{u}^N = \left[u^N_{xx}\ u^N_{yy}\ u^N_{zz}\right]^T$, $\mathbf{\Phi}^M = \left[\Phi^M_{xx}\ \Phi^M_{yy}\ \Phi^M_{zz}\right]^T$ and $\mathbf{\Phi}^N = \left[\Phi^N_{xx}\ \Phi^N_{yy}\ \Phi^N_{zz}\right]^T$. Jump of velocities on the common M and N interface $(I-FRP)$ is linear: therefore, it is necessary to evaluate jump of velocities only on the interface extremes A and B (Fig. 11), as difference between velocities of nodes 1–3 and 2–4 respectively. In particular, if we denote with $\left[x_A\ y_A\ z_A\right]$ point A coordinates, node 1 velocity is given by:

$$\begin{bmatrix}u^1_{xx}\\ u^1_{yy}\\ u^1_{zz}\end{bmatrix} = \begin{bmatrix}u^M_{xx}/(x_A-x_M) & -\Phi^M_{zz} & \Phi^M_{yy}\\ \Phi^M_{zz} & u^M_{yy}/(y_A-y_M) & -\Phi^M_{xx}\\ -\Phi^M_{yy} & \Phi^M_{xx} & u^M_{zz}/(z_A-z_M)\end{bmatrix} \times \begin{bmatrix}x_A-x_M\\ y_A-y_M\\ z_A-z_M\end{bmatrix} = \mathbf{R}_M\left(A-G^M\right) \tag{19}$$

where $G^M = [x_M\ y_M\ z_M]$ denotes the centroid coordinates of element M.

Node 1 velocity can be easily re-written in the $\mathbf{s}^{(k)}-\mathbf{t}^{(k)}-\mathbf{r}^{(k)}$ local interface frame of reference by means of the rotation matrix $\mathbf{T}\left(\vartheta^{(k)}\right)$, where $\vartheta^{(k)}$ is the strip direction with respect to x-axis (Fig. 11):

$$\left[u^1_s\ u^1_r\ u^1_t\right]^T = \mathbf{T}\left(\vartheta^{(k)}\right)\mathbf{R}_M\left(A-G^M\right) \tag{20}$$

No difference occurs for node 2, provided that element N velocities and centroid are used instead of quantities related to M.

Consequently, A jump of velocities is evaluated as:

$$[\mathbf{u}_A] = \mathbf{T}\left(\vartheta^{(k)}\right)\left[\mathbf{R}_M\left(A-G^M\right) - \mathbf{R}_N\left(A-G^N\right)\right] \tag{21}$$

where $[\mathbf{u}_A] = [\Delta u^A_s\ \Delta u^A_r\ \Delta u^A_t]^T = [u^1_s - u^2_s\ u^1_r - u^2_r\ u^1_t - u^2_t]^T$.

Analogous considerations can be repeated for node B, i.e.

$$[\mathbf{u}_B] = \mathbf{T}\left(\vartheta^{(k)}\right)\left[\mathbf{R}_M\left(B-G^M\right) - \mathbf{R}_N\left(B-G^N\right)\right] \tag{22}$$

As already discussed, plastic dissipation is supposed to occur at the interfaces only, due to stresses acting parallel to fibers direction ϑ^k. It is worth noting that such a model is particularly suitable for unidirectional (0°) strips, which may be modelled with truss-like elements (also looking at the Italian code specifications). Nevertheless, no conceptual differences occur introducing a 2D (for instance elliptic) failure criterion for strips.

As a rule, low compressive stresses induce buckling of the strips, due to the FRP negligible thickness. In order to take into account this effect (at least in an approximate way), different limit stresses are assumed in tension and compression, namely f_{FRP}^{+} (assumed equal to f_{fdd} or $f_{fdd,rid}$ in agreement with CNR-DT200 [7], see the following section for details) for tensile failure and $f_{FRP}^{-} \approx 0$ for compression buckling respectively.

To be kinematically admissible, velocity jump at the interfaces [Eqs. (21) and (22)] must comply to the following equality constraints (associated flow rule):

$$[\mathbf{u}_i] = \begin{bmatrix} \Delta u_s^i \\ \Delta u_r^i \\ \Delta u_t^i \end{bmatrix} = \begin{bmatrix} \dot{\lambda}_i^{I-FRP+} - \dot{\lambda}_i^{I-FRP-} \\ 0 \\ 0 \end{bmatrix} \tag{23}$$

where $i = A$ or B and $\dot{\lambda}_i^{I-FRP+}$ and $\dot{\lambda}_i^{I-FRP-}$ are plastic multiplier rates of point i (interface $I - FRP$) corresponding to f_{FRP}^{+} and f_{FRP}^{-} respectively.

On the other hand, from Eqs. (21)–(23), within each interface $I - FRP$ of length L^{I-FRP} (thickness s), the power dissipated may be easily evaluated as:

$$\begin{aligned} \pi^F &= \frac{L^{I-FRP}}{2}\left(\Delta u_s^A \sigma_A + \Delta u_s^B \sigma_B\right) \\ &= \frac{L^{I-FRP}}{2}\left(f_{FRP}^{+}\left(\dot{\lambda}_A^{I-FRP+} + \dot{\lambda}_B^{I-FRP+}\right)\right. \\ &\quad \left. + f_{FRP}^{-}\left(\dot{\lambda}_A^{I-FRP-} + \dot{\lambda}_B^{I-FRP-}\right)\right) \end{aligned} \tag{24}$$

where σ_A and σ_B represent stress action along $\mathbf{s}^{(k)}$ on nodes A and B respectively and all the other symbols have been already introduced.

2.2.3 FRP/masonry interfaces (delamination)

One of the most important aspects in the application of composite materials for strengthening structural elements is the adhesion between the reinforcing and reinforced materials. In particular, when delamination from the support occurs, the effectiveness of the reinforcement vanishes. This phenomenon is very complex to model, especially in the framework of limit analysis, because it involves materials with different properties (masonry, FRP and glue layer) and depends on several parameters. Experimental studies demonstrated that the decohesion occurs due to masonry failure: the delaminated FRP, in fact, presents a consistent layer of masonry material on the debonded surface.

A rigorous methodology to directly take into account in a numerical model the behavior of the layer between masonry and FRP is the use of the interface model concept. According to this model, forces acting on the interface are related to the relative displacement of the two sides (masonry and FRP), thus requiring the utilization of interface elements.

In the Italian technical norm CNR-DT200 [7], a simplified approach is proposed to evaluate the delamination phenomenon, suitably limiting force action on the FRP strip. In particular, the f_{fdd} design tensile strength of FRP elements is:

$$f_{fdd} = \frac{1}{\gamma_{fd}\sqrt{\gamma_M}}\sqrt{\frac{2 \cdot E_{FRP} \cdot \Gamma_{Fk}}{t_{FRP}}} \tag{25}$$

if the so called bond length l_b is greater than the optimal bond length l_e or:

$$f_{fdd,rid} = f_{fdd}\frac{l_b}{l_e}\left(2 - \frac{l_b}{l_e}\right) \tag{26}$$

if $l_b \le l_e$.

In Eqs. (25) and (26) the following symbols have been used:

- $f_{fdd,rid}$, the reduced value of the design bond strength;
- f_{fdd}, the design bond strength;
- E_{FRP}, the FRP Young modulus;
- t_{FRP}, the FRP thickness;
- γ_{fd}, safety factor (it is assumed equal to 1.20 if the reinforcement is applied according to the indications contained in chapter 2 of CNR-DT200 [7], 1.5 otherwise);
- γ_M, partial safety factor for masonry (see Italian D.M. 1987 [30]), assumed in the following equal to 1.0 in order to obtain characteristic values of bond strength;
- l_b, the bond length of FRP elements;
- $l_e = \sqrt{\frac{E_{FRP} \cdot t_{FRP}}{2 \cdot f_{mtm}}}$, the optimal bond length of FRP corresponding to the minimal bond length able to carry the maximum anchorage force (f_{mtm} indicates masonry average tensile strength).

Finally, the term Γ_{Fk} in Eq. (25) represents the characteristic value of the specific fracture energy of the FRP strengthened masonry under a delamination test. In particular, when the debonding involves the first masonry layers, the CNR-DT200 [7] proposes the following relation:

$$\Gamma_{Fd} = c_1\sqrt{f_{mk} \cdot f_{mtm}} \quad [f \ in \ N/mm^2] \tag{27}$$

where c_1 is an experimentally determined coefficient, that typically may range between 0.015/0.030 and f_{mk} is the characteristic value of masonry compressive strength.

The τ_b-slip constitutive law proposed by the document CNR-DT200 [7], see Fig. 12, permits an indirect evaluation of shear limit stress (here denoted with the symbol f_b) to use for masonry/FRP interface elements (and thus avoiding a discretization of FRP strips by means of truss elements with limited strength f_{fdd}), once that the ultimate slip (usually

Fig. 12 Delamination test on masonry specimens **(a)** and bi-linear constitutive relation of the interface FRP-masonry in terms of shear stress (τ_b) and mutual sliding $\bar{s}$ **(b)**

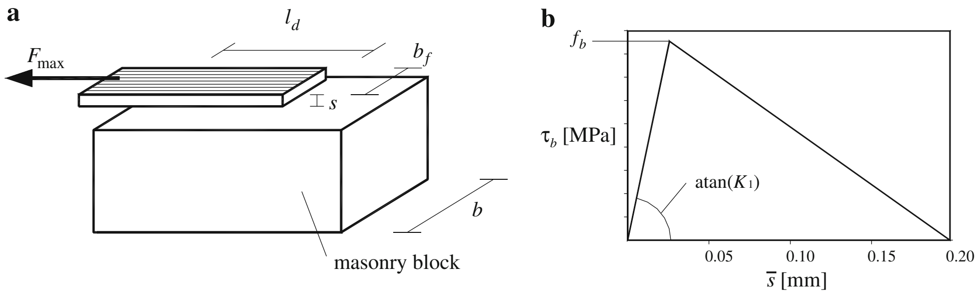

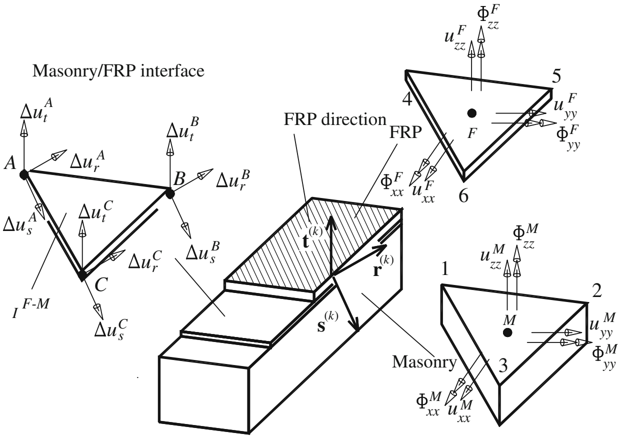

Fig. 13 Masonry-FRP interface jump of displacements

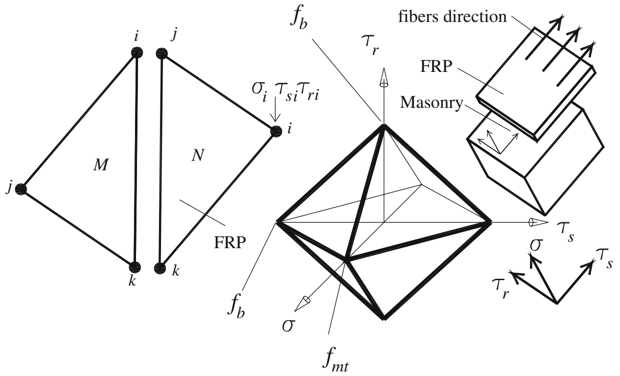

Fig. 14 Masonry-FRP interface linearized failure surface

fixed at 0.2 mm) is known (area under the τ_b-slip constitutive law of Fig. 12 is Γ_{Fd}).

Let us consider a triangular FRP-masonry interface I^{M-F} between elements F (FRP) and M (masonry), as depicted in Fig. 13.

$\mathbf{u}^F = \left[u_{xx}^F\ u_{yy}^F\ u_{zz}^F\right]^T$ and $\mathbf{u}^M = \left[u_{xx}^M\ u_{yy}^M\ u_{zz}^M\right]^T$ indicate F and M centroids velocities respectively, whereas $\boldsymbol{\Phi}^F = \left[\Phi_{xx}^F\ \Phi_{yy}^F\ \Phi_{zz}^F\right]^T$ and $\boldsymbol{\Phi}^M = \left[\Phi_{xx}^M\ \Phi_{yy}^M\ \Phi_{zz}^M\right]^T$ F and M rotation rates vectors.

Jump of velocities on the common I^{M-F} interface is linear and may be evaluated on nodes A, $B$and C of the interface (Fig. 13) as difference between velocities of nodes 1–4 and 2–5 and 3–6 respectively. In particular, if $[x_A\ y_A\ z_A]$ represents point A coordinates, velocity of node 1 is given by:

$$\begin{bmatrix} u_{xx}^1 \\ u_{yy}^1 \\ u_{zz}^1 \end{bmatrix} = \begin{bmatrix} u_{xx}^M/(x_A - x_M) & -\Phi_{zz}^M & \Phi_{yy}^M \\ \Phi_{zz}^M & u_{yy}^M/(y_A - y_M) & -\Phi_{xx}^M \\ -\Phi_{yy}^M & \Phi_{xx}^M & u_{zz}^M/(z_A - z_M) \end{bmatrix} \times \begin{bmatrix} x_A - x_M \\ y_A - y_M \\ z_A - z_M \end{bmatrix} = \mathbf{R}_M (A - G^M) \tag{28}$$

where $G^M = [x_M\ y_M\ z_M]$ is the centroid of masonry element M.

As already discussed in the previous section, node 1 velocity in the local $\mathbf{s}^{(k)} - \mathbf{t}^{(k)} - \mathbf{r}^{(k)}$ frame of reference is:

$$\left[u_s^1\ u_r^1\ u_t^1\right] = \mathbf{T}\left(\vartheta^{(k)}\right)\mathbf{R}_M\left(A - G^M\right) \tag{29}$$

Equation (29) can be re-written for node 4, substituting M quantities with F quantitites.

Thus, jump of velocity on A can be evaluated as:

$$[\mathbf{u}_A] = \mathbf{T}\left(\vartheta^{(k)}\right)\left[\mathbf{R}_M\left(A - G^M\right) - \mathbf{R}_F\left(A - G^F\right)\right] \tag{30}$$

where $[\mathbf{u}_A] = [\Delta u_s^A\ \Delta u_r^A\ \Delta u_t^A]^T = [u_s^1 - u_s^4\ u_r^1 - u_r^4\ u_t^1 - u_t^4]^T$ indicates the jump of velocities on A in the local coordinate system.

No conceptual differences occur for nodes B and C, therefore Eq. (30) can be utilized for all the vertices of the triangular interface.

To be kinematically admissible, jump of displacement field at the $F - M$ interfaces must obey an associated flow rule. A linearization of $F - M$ failure surface in the form $A_k\tau_{si} + B_k\tau_{ri} + C_k\sigma_i = D_k, k = 1, \ldots, N_{PL}^{M-F}$ (N_{PL}^{M-F} is the number of planes used in the linearization of the failure surface, σ_i, τ_{si} and τ_{ri} aredefined in Fig. 14) is assumed.

Fig. 15 Mosallam [22] masonry wall in cylindrical flexion. Deformed shapes at collapse. **a** un-strengthened. **b** FRP strengthened

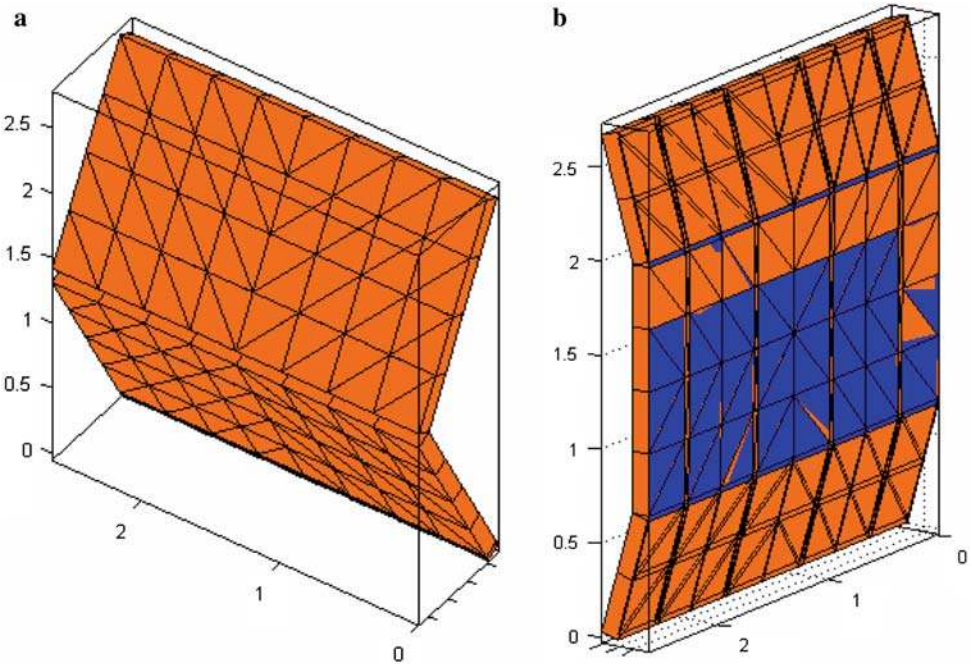

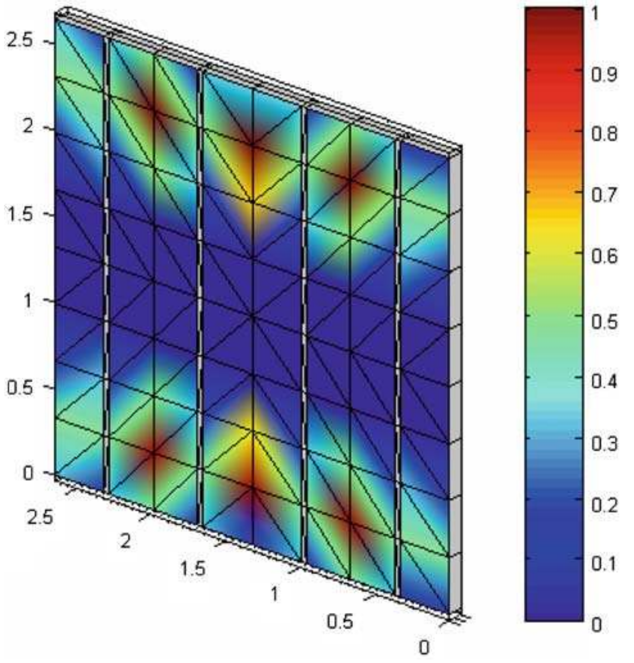

Fig. 16 Mosallam [22] masonry wall in cylindrical flexion. FRP-masonry interface normalized dissipation patch

In the framework of associated limit analysis, the following equality constraints must be imposed:

$$[\mathbf{u}_i] = \begin{bmatrix} \Delta u_s^i \\ \Delta u_r^i \\ \Delta u_t^i \end{bmatrix} = \begin{bmatrix} \sum_{k=1}^{N_{PL}^{M-F}} A_k \dot{\lambda}_i^{M-F,k} \\ \sum_{k=1}^{N_{PL}^{M-F}} B_k \dot{\lambda}_i^{M-F,k} \\ \sum_{k=1}^{N_{PL}^{M-F}} C_k \dot{\lambda}_i^{M-F,k} \end{bmatrix} \tag{31}$$

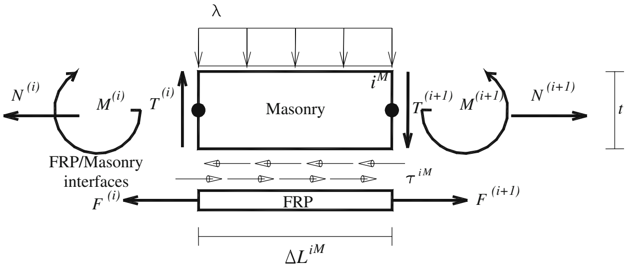

Fig. 17 Basic assumptions adopted for the LB 1D limit analysis model

where $i = A, B$ or C, $\dot{\lambda}_i^{M-F,k}$ is the kth plastic multiplier rate corresponding to the kth plane. The Italian CNR-DT200 [7] provides $\sigma - \tau_s - \tau_r$ failure surfaces for masonry/FRP interfaces, see Fig. 14, where f_{mt} represents masonry tensile strength and f_b is the interface shear strength.

From Eqs. (29)–(31), within each interface $F - M$ of area A^I, the power dissipated may be easily evaluated as:

$$\begin{aligned} \pi^{F-M} &= \frac{A^I}{3}\left(\sum_{i=A}^{C}\left(\Delta u_t^i \sigma_i + \Delta u_s^i \tau_{si} + \Delta u_r^i \tau_{ri}\right)\right) \\ &= \frac{A^I}{3}\sum_{i=1}^{3}\sum_{k=1}^{N_{PL}^{M-N}} \dot{\lambda}_i^{M-F,k} D_k \end{aligned} \tag{32}$$

2.2.4 The linear programming problem at a structural level

External power can be written as $P^{ex} = (\mathbf{P}_0^T + \lambda \mathbf{P}_1^T)\mathbf{U}$, where $\mathbf{P}_0$ is the vector of (equivalent lumped) permanent loads, λ is the load multiplier, $\mathbf{P}_1^T$ is the vector of (lumped)

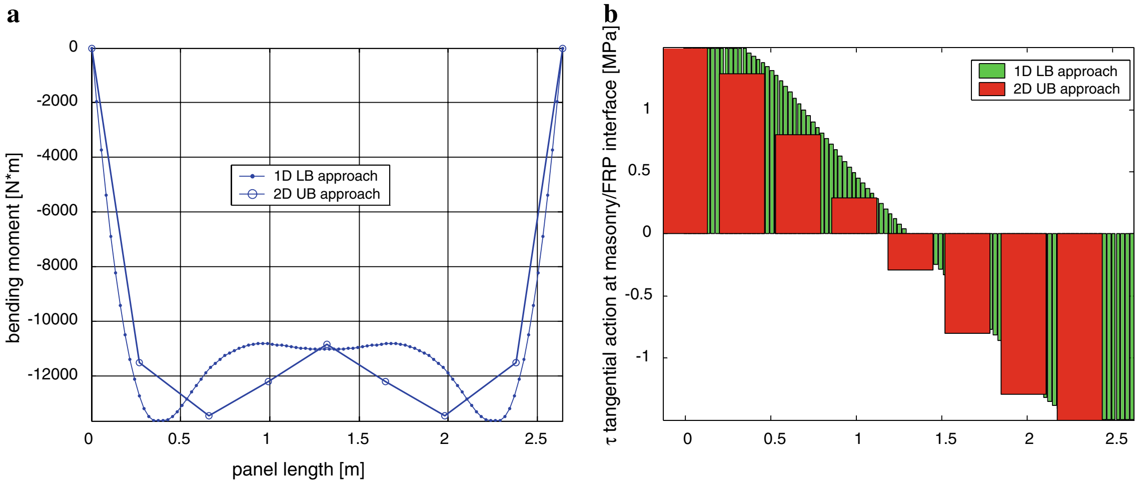

Fig. 18 Comparison between 1D LB approach and 2D UB dual approach **a** Bending moment (in masonry sections) evaluation along wall length. **b** FRP-masonry interface tangential actions

Fig. 19 Geometry of masonry slabs analyzed

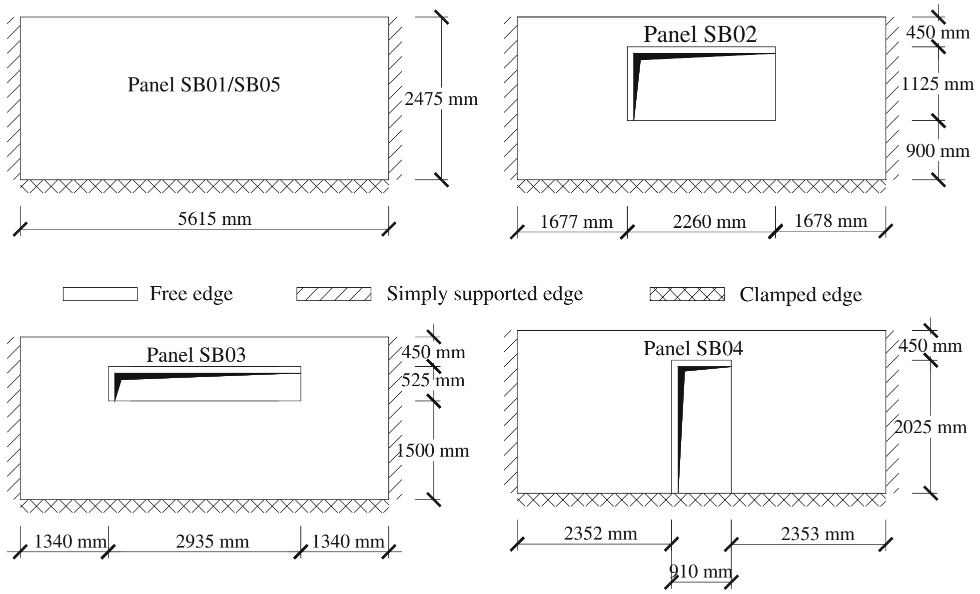

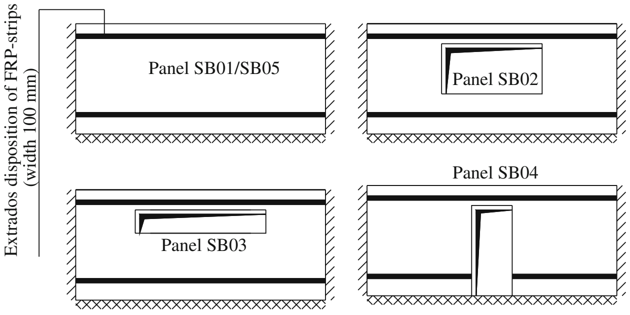

Fig. 20 FRP strips disposition

variable loads and $\mathbf{U}$ is the vector of assembled nodal velocities. As the amplitude of the failure mechanism is arbitrary, a further normalization condition $\mathbf{P}_1^T\mathbf{U} = 1$ is usually introduced to solve the limit analysis problem within LP. In this way, the external power becomes linear in $\mathbf{w}$ and λ, i.e. $P^{ex} = \mathbf{P}_0^T\mathbf{w} + \lambda$.

After some elementary assemblage operations, a simple linear programming problem is obtained (analogous to that reported in [31]), where the objective function to minimize is the total internal dissipation minus external power of loads independent from λ:

$$\begin{cases} \min\ \left\{\pi^{M,ass}\left(\dot{\lambda}^{M,ass}\right) + \pi^{F,ass}\left(\dot{\lambda}^{F,ass}\right) \right. \\ \qquad \left. + \pi^{M-F,ass}\left(\dot{\lambda}^{M-F,ass}\right) - \mathbf{P}_0^T\mathbf{U}\right\} \\ \text{such that} \begin{cases} \mathbf{A}^{eq}\mathbf{U} = \mathbf{b}^{eq} \\ \mathbf{P}_1^T\mathbf{U} = 1 \\ \dot{\lambda}^{M,ass} \geq \mathbf{0} \\ \dot{\lambda}^{F,ass} \geq \mathbf{0} \\ \dot{\lambda}^{M-F,ass} \geq \mathbf{0} \end{cases} \end{cases} \tag{33}$$

Fig. 21 Chong et al. experimental tests. Comparison between experimental and numerical results (no reinforcement)

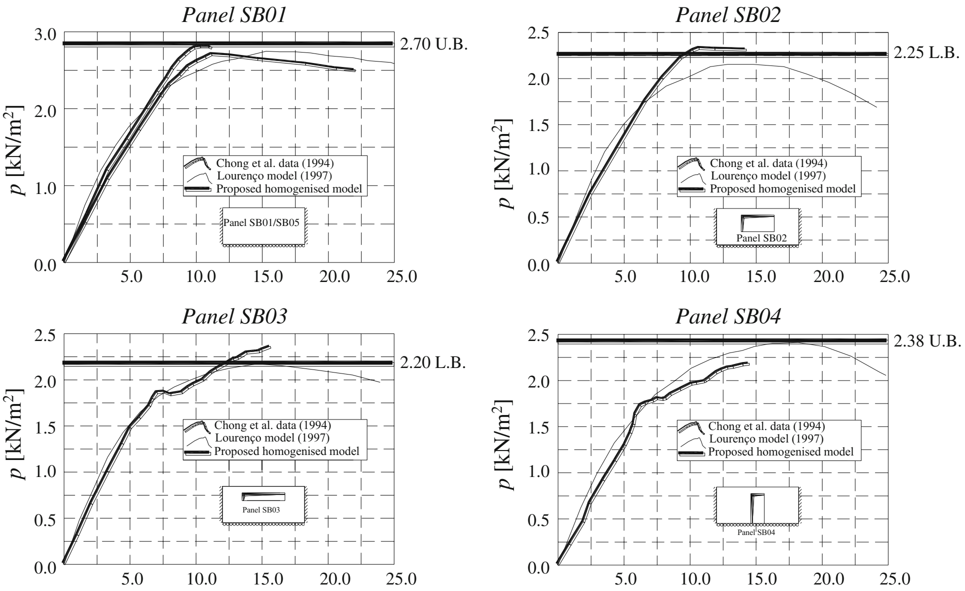

Fig. 22 Chong et al. experimental tests. Increase of the ultimate out-of-plane pressure varying f_b (**a** panel SB01/SB05. **b** panel SB02. **c** panel SB03. **d** panel SB04)

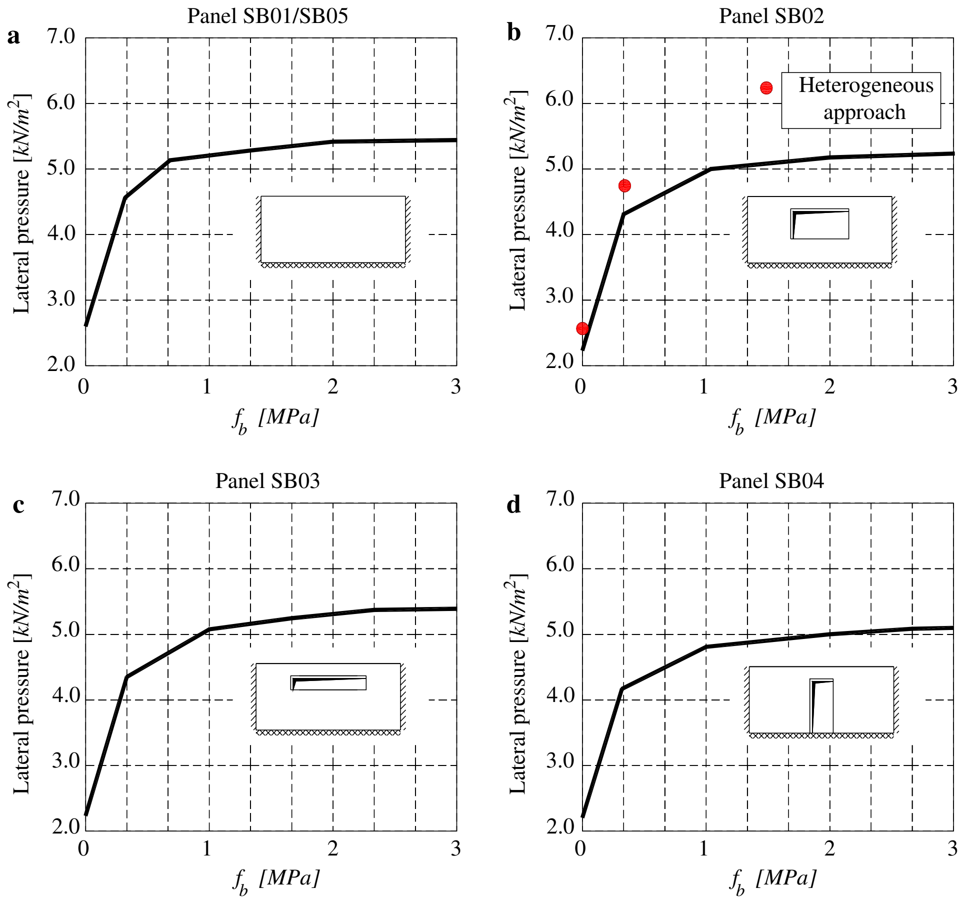

where:

- $\pi^{M,ass}$, $\pi^{F,ass}$ and $\pi^{M-F,ass}$ are respectively the internal dissipation on masonry interfaces (M), on FRP interfaces (F) and on masonry/FRP interfaces ($M-F$).
- $\mathbf{U} = [\mathbf{u}^{M,ass}\ \mathbf{\Phi}^{M,ass}\ \dot{\boldsymbol{\lambda}}^{M,ass}\ \mathbf{u}^{F,ass}\ \mathbf{\Phi}^{F,ass}\ \dot{\boldsymbol{\lambda}}^{F,ass}\ \dot{\boldsymbol{\lambda}}^{M-F,ass}]^T$ is the vector of global unknowns, collecting the vector of assembled centroids masonry elements velocities ($\mathbf{u}^{M,ass}$) and rotation rates ($\mathbf{\Phi}^{M,ass}$), the vector of assembled masonry interfaces multipliers rates

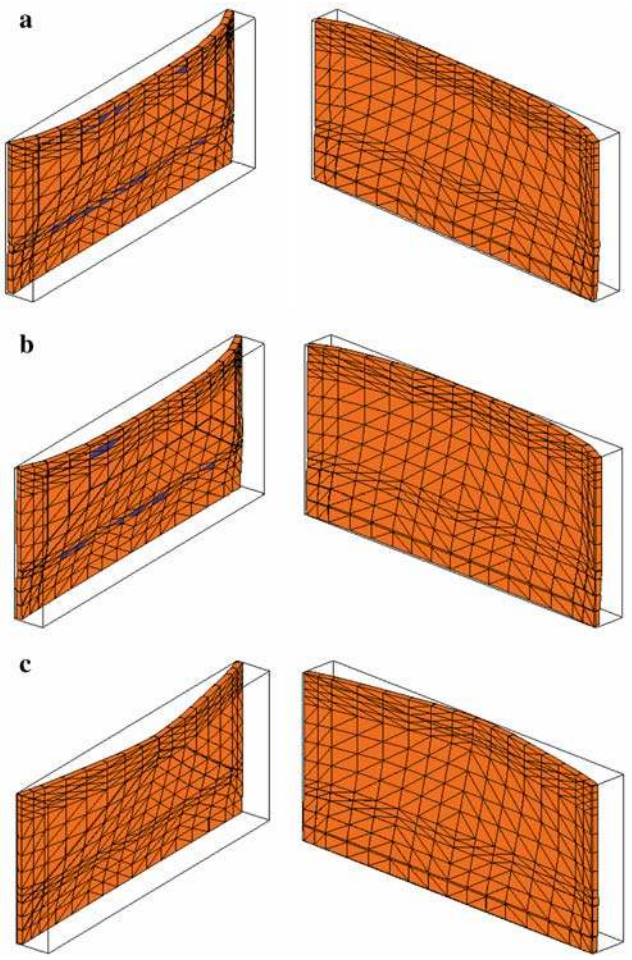

Fig. 23 Chong et al. experimental tests, panel SB01. Deformed shape at collapse for three different values of strips tangential adhesion (**a** $f_b = 3\,\text{MPa}$; **b** $f_b = 0.3\,\text{MPa}$; **c** unreinforced case)

($\dot{\boldsymbol{\lambda}}^{M,ass}$), the vector of assembled centroids FRP elements velocities ($\mathbf{u}^{F,ass}$) and rotation rates ($\boldsymbol{\Phi}^{F,ass}$), the vector of assembled FRP interfaces multipliers rates ($\dot{\boldsymbol{\lambda}}^{F,ass}$) and the vector of assembled FRP/masonry interfaces multipliers rates ($\dot{\boldsymbol{\lambda}}^{M-F,ass}$)

- $\mathbf{A}^{eq}$ is the overall equality constraints matrix and cosllects velocity boundary conditions [Eq. (18)], relations between jump of velocities on interfaces and elements velocities and associated plastic flow constraints on discontinuities [i.e. Eqs. (15), (16), (21)–(23), (30) and (31)].

It is worth noting that recent trends in limit analysis have demonstrated that the linearization of the strength domain can be circumvented using conic/semidefinite programming (e.g. [32–34]). However, since the aim of this paper is mainly devoted to structural aspects of the problem, classic interior point LP routines available in Matlab are used for the sake of simplicity.

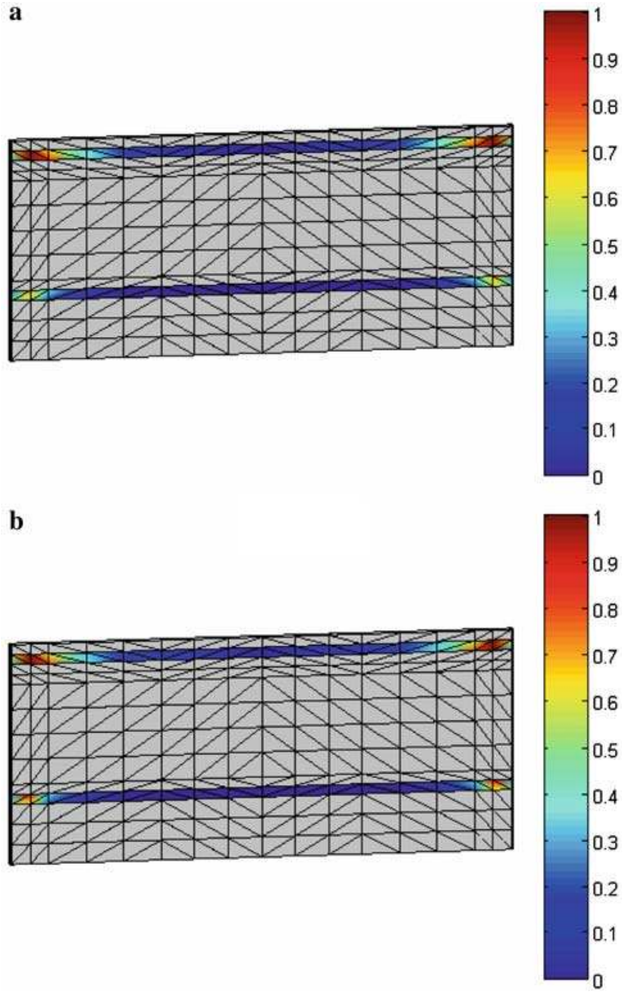

Fig. 24 Chong et al. experimental tests, panel SB01. Strips normalized delamination patch (**a**: $f_b = 3\,\text{MPa}$; **b** $f_b = 0.3\,\text{MPa}$)

3 Structural examples

The first numerical simulations set refers to a simply supported FRP reinforced masonry panel in cylindrical flexion experimentally and theoretically analyzed by Mosallam [22]. Both for the unreinforced and FRP-reinforced case, results obtained with the present model fit well experimental data presented by Mosallam [22]. Finally, numerical data are compared with those resulting from a simple one-dimensional static limit analysis procedure.

The second example focuses on four masonry walls in two-way bending with and without openings and differently constrained at the edges. Such walls have been already analyzed experimentally and numerically by Chong et al. [23], Lourenço [18] and Milani et al. [13] in absence of FRP reinforcement. On the other hand, it is worth noting that, at present, there is still a lack both of experimental data and numerical models concerning strengthened masonry walls in two-way bending. In the numerical simulations, strips are

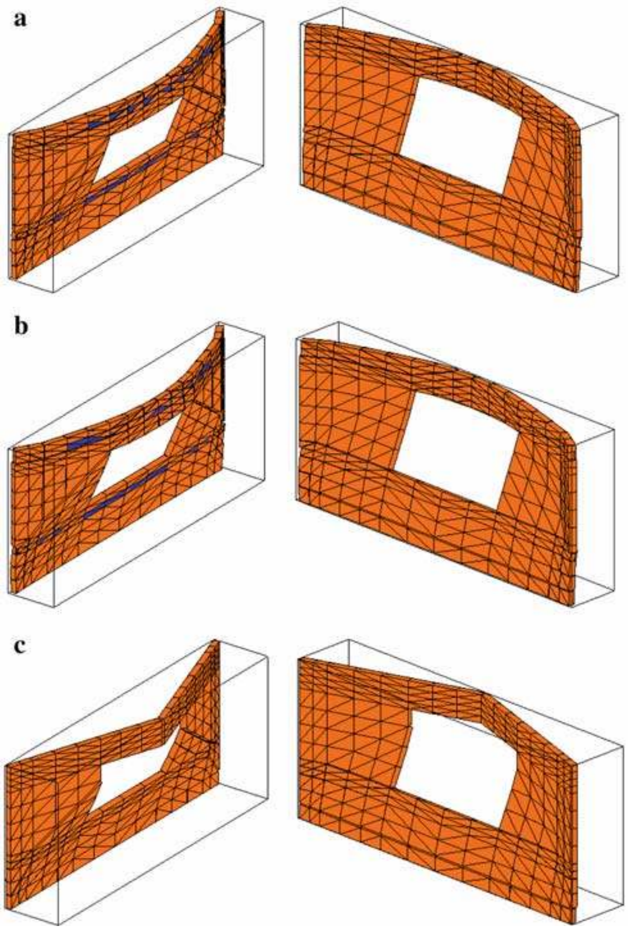

Fig. 25 Chong et al. experimental tests, panel SB02, reinforcement with horizontal strips. Deformed shape at collapse for three different values of strips tangential adhesion (**a** $f_b = 3\,\text{MPa}$; **b** $f_b = 0.3\,\text{MPa}$; **c** unreinforced case)

disposed in such a way to preclude the formation of typical vertical and inclined cylindrical hinges, forming the failure mechanism in the unreinforced case. Due to the fact that no reference results are available from the literature for the strengthened panels, only the increase of the ultimate out-of-plane strength is estimated.

3.1 Simply supported reinforced panels in cylindrical flexion

A FRP reinforced red brick masonry wall in cylindrical flexion experimentally tested by Mosallam [22] is here analyzed with the numerical model proposed. The wall is square with an edge length equal to 2.64 m, thickness $t = 10.16\,\text{cm}$. The specimen is simply supported on two edges parallel to bed joints. The panel is also retrofitted at the extrados by means of discontinuous contiguous carbon/epoxy strips. All specimens were tested by Mosallam [22] in a water-bag structural frame in order to apply a uniform hydraulic pressure on the wall until ultimate failure occurred. Common red clay bricks of dimensions $20.3210.16 \times 5.72\,\text{cm}^3$ were used. Only compression tests on single bricks and masonry pillars were conducted by Mosallam [22] for the mechanical characterization of masonry, providing respectively an ultimate strength equal to 16 and 25 MPa.

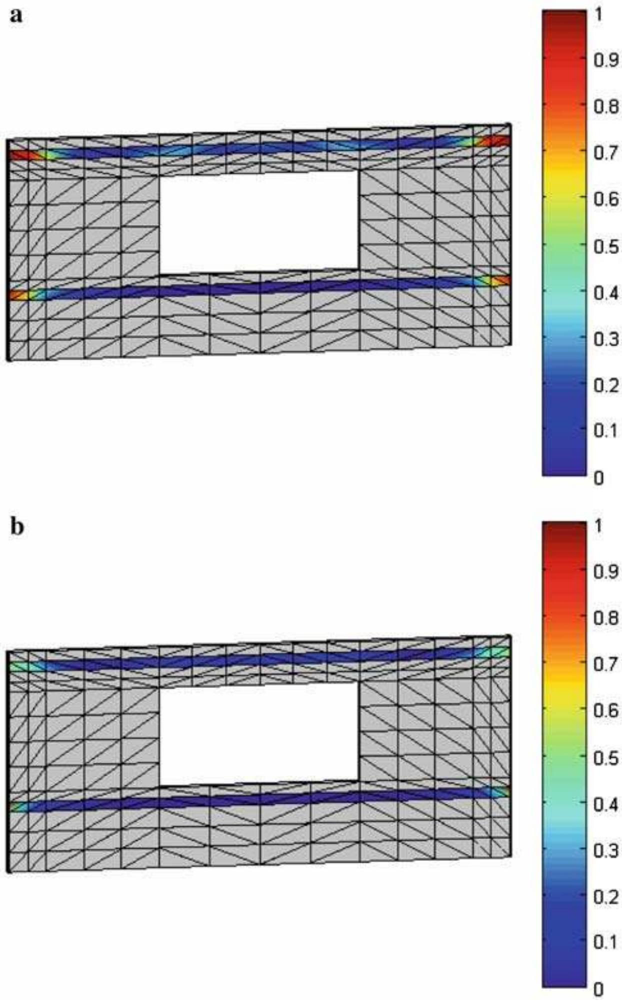

Fig. 26 Chong et al. experimental tests, panel SB02, reinforcement with horizontal strips. Strips normalized delamination patch (**a** $f_b = 3\,\text{MPa}$; **b** $f_b = 0.3\,\text{MPa}$)

No experimental information is given on the tensile masonry behavior in flexion. In order to suitably calibrate input mechanical properties of the constituent materials, for mortar joints a typical value of f_t tensile strength equal to $1/15 f_c$ is assumed. Furthermore, a Lourenço and Rots [17] failure criterion is adopted with cohesion $c = f_t$, friction angle $\Phi = 30°$, $\Phi_2 = 90°$ (shape of the linearized compressive cap) and compressive strength f_c equal to 16 MPa (see also Fig. 6). It is interesting to notice that mortar compressive strength is kept equal to masonry one, since the model proposed is unable to reproduce the typical three-dimensional failure of bricks, which are assumed as infinitely resistant.

Fig. 27 Chong et al. experimental tests, panel SB02, heterogeneous approach. Deformed shape at collapse for **a** $f_b = 0.3\,\text{MPa}$ and **b** unreinforced case

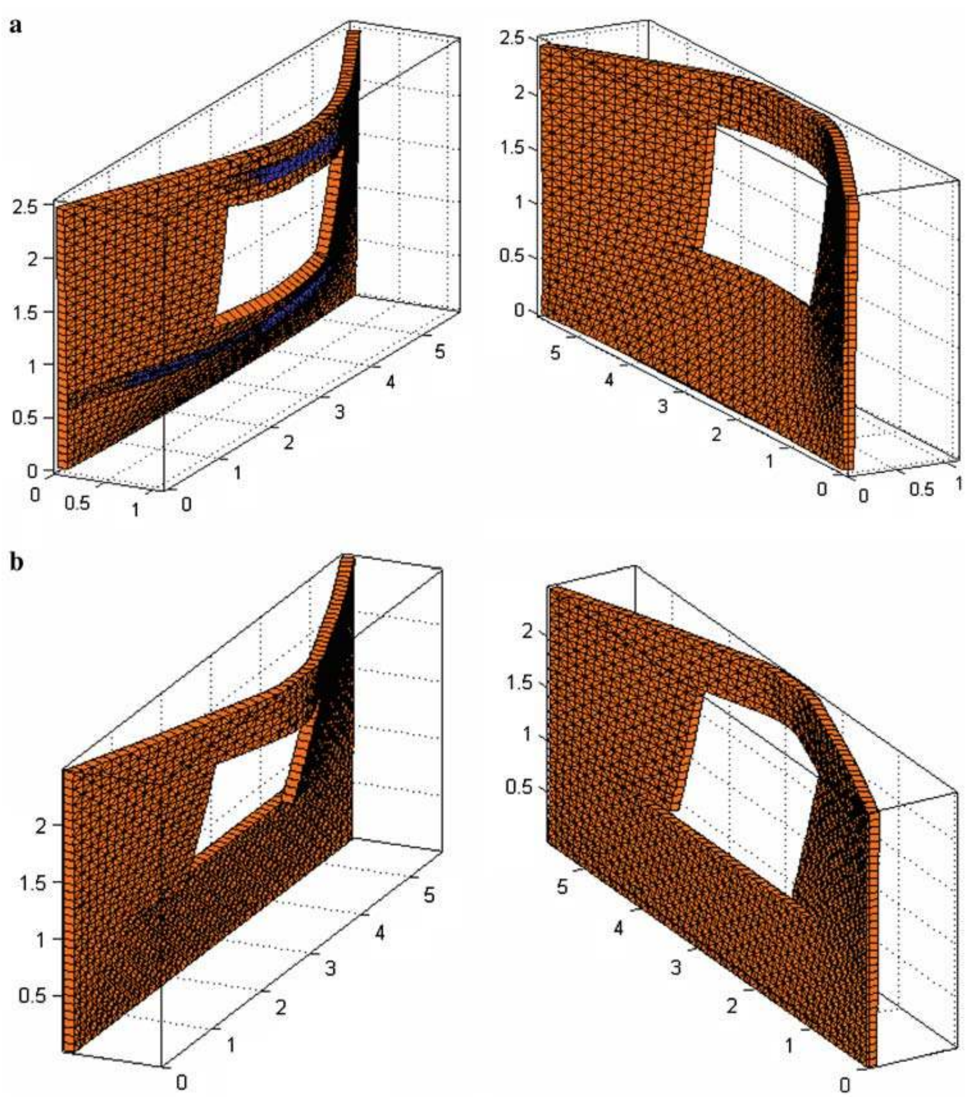

f_b bond shear strength is assumed equal to 1.5 MPa. It is worth underling that, in order to obtain a continuous reinforcement on the whole extrados, contiguous strips with unspecified width were used by Mosallam [22]. Three different strengthening technologies were analyzed in [22], corresponding to (I) unidirectional $(0°)_2$ carbon/epoxy, (II) bi-directional $(0° - 90°)_1$ and unidirectional $(0°)_3$ E-glass/epoxy strips. In the present paper, only configuration (I) is analyzed. In order to suitable take into account that contiguous strips are not physically connected, in the model a mesh with small offsets of the nodes belonging to strips edges is utilized (see Fig. 15).

In Fig. 15, the deformed shapes at collapse of the un-strengthened (a) and strengthened (b) panels are compared. Furthermore, in Fig. 16 normalized power dissipation at the FRP/masonry bond obtained in presence of FRP is depicted. As expected, for the un-strengthened wall, failure occurs for the formation of a central plastic hinge on the bed joint (Fig. 15a). On the contrary, the FRP reinforced panel collapses with the formation of two plastic hinges in correspondence of the maximum bending moment and with a diffused delamination of the strips near the extremes. It is worth underling that, contrarily to the unreinforced case, masonry maximum bending moment is not reached in the symmetry section of the wall, due to tangential stresses acting at the interfaces between masonry and FRP.

Collapse failure loads numerically obtained are 5.93 and 79.51 kPa respectively for the un-reinforced and the FRP-reinforced panel. Numerical results are in good agreement with Mosallam experimental data (5.98 and 74.4 kPa results).

In order to compare numerical results with alternative approaches, a 1D lower bound limit analysis model have been also developed. In a one-dimensional framework, masonry is modeled by means of Timoshenko beam elements with finite bending/out-of-plane shear resistance, whereas FRP strips are meshed with truss elements (see Fig. 17). Each masonry element i^M connects nodes (i) and $(i+1)$. For each node, optimization variables $M^{(i)}$, $T^{(i)}$, $N^{(i)}$ and $F^{(i)}$ are introduced, corresponding respectively to masonry bending moment, masonry out of plane shear, masonry axial load and FRP normal action. FRP and masonry interact by means of tangential stresses τ^{i^M} at the common interfaces.

Equilibrium equations for each element can be summarized as follows:

$$\begin{array}{ll} (a) & M^{(i+1)} - M^{(i)} - T^{(i+1)}\Delta L^{i^M} \\ & -\tau^{i^M}\Delta L^{i^M} t/2 - \lambda\left(\Delta L^{i^M}\right)^2/2 = 0 \\ (b1) & T^{(i)} - T^{(i+1)} - \lambda\Delta L^{i^M} = 0 \\ (b2) & N^{(i+1)} - N^{(i)} - \tau^{i^M}\Delta L^{i^M} = 0 \\ (c) & F^{(i+1)} - F^{(i)} + \tau^{i^M}\Delta L^{i:M} = 0 \end{array} \tag{34}$$

Equation (a) represents rotation equilibrium of masonry elements, equations (b) translation equilibrium of masonry elements on perpendicular directions and equation (ct) translation equilibrium of FRP.

In addition, inequality constraints have to be introduced for each node of the mesh on masonry, FRP and masonry/FRP interface elements, in order to ensure admissibility of internal actions.

It is worth underlining that a linearization of masonry failure surface for each node (i) in the form $A_k M^{(i)} + B_k T^{(i)} + C_k N^{(i)} = 1$ is required, where k indicates the k^{th} linearization plane. Such a linearization is at disposal from the homogenization procedure described in the previous sections.

Equilibrium equations and admissibility of internal actions lead, after suitable assemblage operations, to the following standard lower bound linear programming problem:

$$\max\{\lambda\} \text{ such that } \begin{cases} \mathbf{A}^{eq}\mathbf{X} = \mathbf{b}^{eq} \\ \mathbf{A}^{in}\mathbf{X} \leq \mathbf{b}^{in} \end{cases} \tag{35}$$

where assembled vector $\mathbf{X}$ collects masonry bending moments $M^{(i)}$, masonry out-of-plane shears $T^{(i)}$, masonry axial actions $N^{(i)}$, interface tangential actions τ^{i^M}, FRP normal actions $F^{(i)}$ and collapse external load λ.

In order to compare results obtained via the 2D upper bound approach proposed in this paper with results from Eq. (35), we exploit the duality theorem of limit analysis, which allows to have an estimation of static internal actions corresponding to the UB solution, i.e.:

$$\begin{cases} \min\left\{-\mathbf{P}_0^T\mathbf{U} + \pi^{ass}\dot{\lambda}^{ass}\right\} \\ \text{such that } \begin{cases} \mathbf{H}^T\mathbf{U} + \mathbf{A}^{in^T}\dot{\lambda}^{ass} = \mathbf{0} \\ \mathbf{P}_1^T\mathbf{U} = 1 \\ \dot{\lambda}^{ass} \geq \mathbf{0} \\ \text{primal} \end{cases} \end{cases} \begin{cases} \max\left\{\hat{\lambda}\right\} \\ \text{such that } \begin{cases} \mathbf{H}\boldsymbol{\Sigma} + \mathbf{R}\hat{\lambda} - \mathbf{P}_0 = 0 \\ \mathbf{A}^{in}\boldsymbol{\Sigma} \leq \pi^{assT} \\ \text{dual} \end{cases} \end{cases} \tag{36}$$

where Σ at the solution point collects masonry, FRP and masonry/FRP internal actions at collapse.

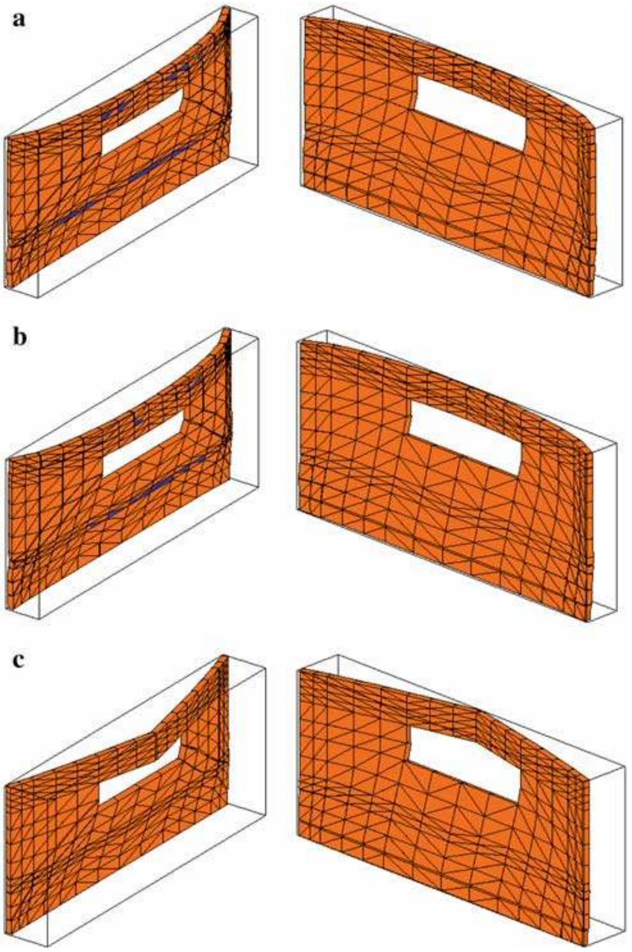

Fig. 28 Chong et al. experimental tests, panel SB03, reinforcement with horizontal strips. Deformed shape at collapse for three different values of strips tangential adhesion (**a** $f_b = 3\,\text{MPa}$; **b** $f_b = 0.3\,\text{MPa}$; **c** unreinforced case)

In Fig. 18, bending moment distribution (a) and bond tangential actions (b) at collapse obtained via both models proposed [Eqs. (35) and (36)] are depicted. The slight differences between models depend only on the mesh utilized, which is coarser for the bi-dimensional case (see Fig. 15). For the one-dimension approach, a subdivision with 100 elements is utilized. The good agreement between results shows that reliable predictions can be obtained, also in the monodimensional case, with the 2D homogenization model proposed.

3.2 Reinforced panels in two way bending

Experimental tests on five unreinforced solid clay panels (labeled from SB01 to SB05) with and without openings were carried out by Chong et al. [23], (see also [18]). Panels SB01 and SB05 are replicates and, therefore, only four different configurations are tested. Each panel, with dimensions

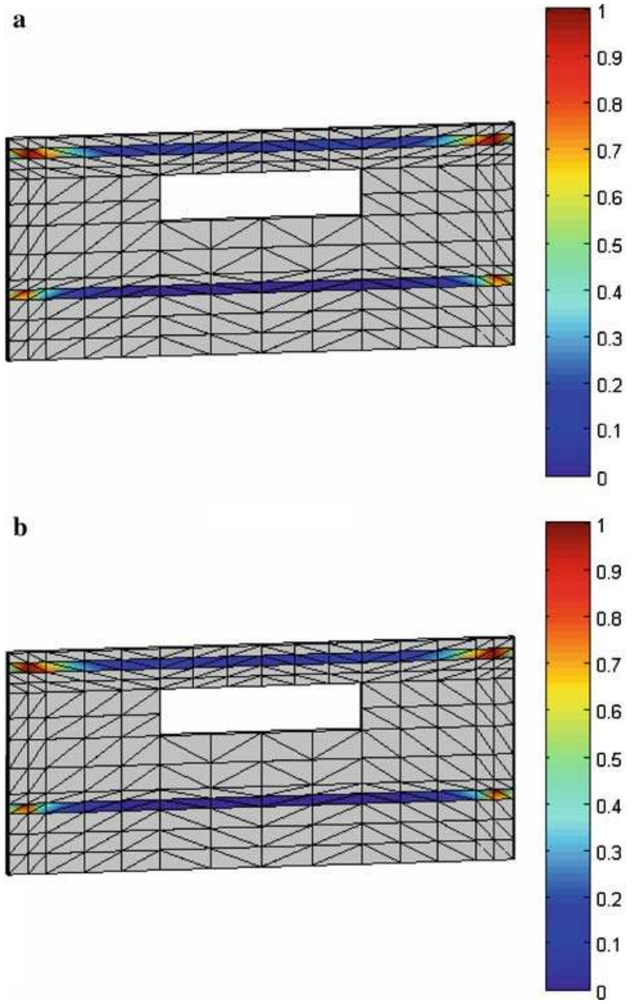

Fig. 29 Chong et al. experimental tests, panel SB03, reinforcement with horizontal strips. Strips normalized delamination patch (**a** $f_b = 3\,\text{MPa}$; **b** $f_b = 0.3\,\text{MPa}$)

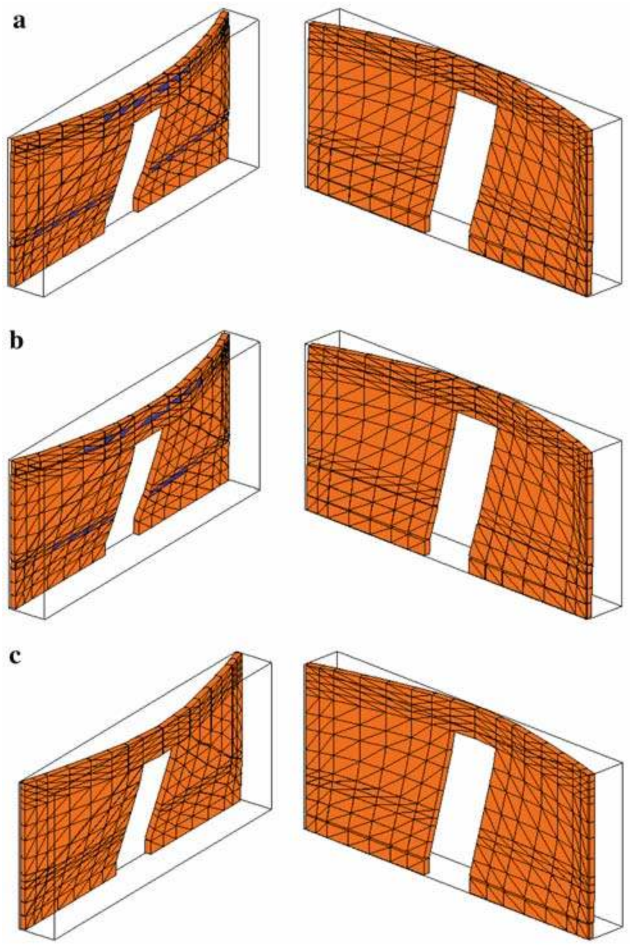

Fig. 30 Chong et al. experimental tests, panel SB04, reinforcement with horizontal strips. Deformed shape at collapse for three different values of strips tangential adhesion (**a** $f_b = 3\,\text{MPa}$; **b** $f_b = 0.3\,\text{MPa}$; **c** unreinforced case)

$5600 \times 2475 \times 102.5\,\text{mm}^3$, was built in stretcher bond between two stiff abutments with the vertical edges simply supported (allowance for in-plane displacements was provided) and the top edge free. A completely restrained support was provided at the base. All opening sizes and dimensions used in the tests are sketched in Fig. 19.

No experimental data are available from the literature concerning such panels in presence of FRP reinforcement. In this section, both the unreinfoced and the FRP strengthened case are considered. When dealing with the reinforced case, two horizontal strips with width 100 mm are disposed on the extrados of the walls in correspondence of the top and at the base, with the aim of precluding the formation of vertical and inclined yield lines observed both experimentally and numerically on the URM panels. In Fig. 20, a sketch the FRP strips dimensions and disposition assumed in the numerical simulations is reported.

The ultimate strength increase and the changes in the failure mechanisms obtained are evaluated in what follows.

The panels were loaded by air-bags until failure with increasing out-of-plane uniform pressure p. The air pressure and the displacement d for the middle point of the free edge were monitored during testing. Mechanical properties assumed for mortar joints are reported in Table 1. The reader is also referred to the previous section, where masonry homogenized failure surface obtained with the micro-mechanical approach proposed is reported.

In Fig. 21, collapse loads obtained with the present model for all the unreinforced walls are represented. Experimental pressure-displacement curves by Chong et al. [23], and numerical curves obtained by means of an orthotropic elasto-plastic macro-model by Lourenço [18] are also depicted. As it is possible to notice, a comparison among all the results shows that the limit analysis approach proposed is able to provide ultimate loads in good agreement both with experimental data and with alternative elasto-plastic models.

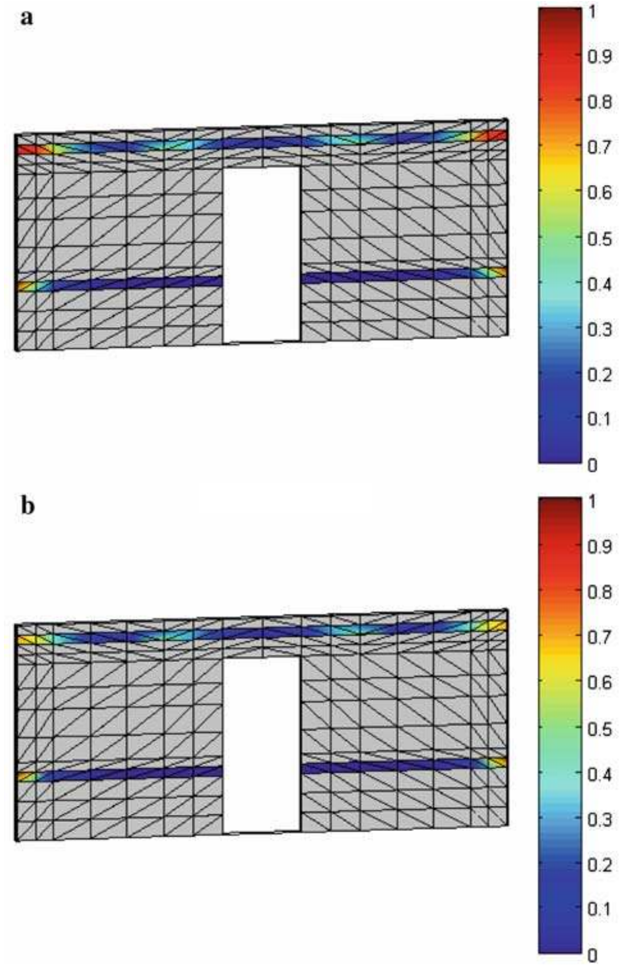

Fig. 31 Chong et al. experimental tests, panel SB04, reinforcement with horizontal strips. Strips normalized delamination patch (**a** $f_b = 3\,\text{MPa}$; **b** $f_b = 0.3\,\text{MPa}$)

In Fig. 22, the increase of ultimate loads in presence of FRP and varying f_b masonry/FRP interface strength in a wide range (from 0 to 3 MPa) is represented. As it is possible to notice, collapse load reaches asymptotically a maximum for high f_b values for all the panels analyzed, meaning that the optimal benefit that can be obtained from a strengthening intervention is limited to a specific f_b range (namely between 0.3 and 0.8 MPa). Nevertheless, as already discussed, it is worth noting that the correct evaluation of f_b remains an open issue: therefore, a sensitivity analysis should be always performed to evaluate strengthening efficiency.

In Fig. 23, panel SB01 deformed shapes at collapse with and without FRP reinforcement are represented. Three different deformed shapes are depicted, corresponding to a f_b masonry/FRP bond strength respectively equal to 3 MPa (a), 0.3 MPa (b) and 0 MPa (c, i.e. unreinforced case). In Fig. 24, the normalized power dissipation patch at the masonry/FRP interface for f_b equal to 3 MPa (a) and 0.3 MPa (b) is depicted. As can be deduced from the figure, a diffused delamination of the strips occurs in correspondence of the extremes, in agreement both with experimental evidences and Italian norm specifications. Furthermore, deformed shapes at collapse reported in Fig. 23 clearly show that failure mechanism remains essentially unchanged passing from $f_b = 0.3$ to $f_b = 3\,\text{MPa}$, hence confirming the negligible increase of the ultimate pressure. On the other hand, from Fig. 23 an evident change in the failure mechanism can be observed between the reinforced and the unreinforced case (compare for instance Fig. 23a, c), confirming that strips act as ties which tend to preclude the formation of cylindrical hinges on masonry.

Analogously to the previous case, in Figs. 25 and 26 homogenized results for panel SB02 are reported. In order to show the capabilities of the numerical model proposed, in Fig. 27 deformed shapes at collapse obtained using a heterogeneous approach (i.e. meshing separately bricks and mortar joints reduced to interfaces, assuming bricks infinitely resistant) in the unreinforced case and with $f_b = 0.3\,\text{MPa}$ are reported. Corresponding failure loads are represented with red dots in Fig. 22. While failure mechanisms and failure loads are very similar to those provided by the homogenized model, time required for the simulations on a PC Intel Celeron 1.40 GHz equipped with 1Gb RAM exceeded 2 hours, a processing effort around 10^2 times grater with respect to that required by homogenized models. Finally, homogenization allows to sensibly reduce pre-processing time, especially in the general case of strips inclined with respect to bed joints.

The same results reported for panel SB01 and SB02 are replicated in Figs. 28, 29, 30 and 31 for panels SB03 (Figs. 28, 29) and SB04 (Figs. 30, 31). Analogously to panel SB01 and SB02 data, for all the other walls analyzed, numerical results confirm the important role played by f_b parameter on the evaluation of walls ultimate out-of-plane strength (Fig. 22b–d). Delamination occurs in any case at the extremes of the strips and failure mechanisms of the wall change considerably when a horizontal strengthening with adequate f_b is introduced.

References

1. Spence R, Coburn A (1992) Strengthening building of stone masonry to resist earthquakes. Meccanica 27:213–221
2. Korany Y, Drysdale R (2007) Load-displacement of masonry panels with unbonded and intermittently bonded FRP. I: analytical model. J Compos Constr 11(1):15–23
3. Korany Y, Drysdale R (2007) Load-displacement of masonry panels with unbonded and intermittently bonded FRP. II: analytical study. J Compos Constr 11(1):24–32
4. Page AW (1981) A biaxial failure criterion for brick masonry in the tension-tension range. Int J Mason 1:26–30
5. Milani G, Lourenço PB, Tralli A (2006) Homogenised limit analysis of masonry walls. Part I: failure surfaces. Comput Struct 84(3–4):166–180

6. Luciano R, Sacco E (1998) Damage of masonry panels reinforced by FRP sheets. Int J Solids Struct 35(15):1723–1741
7. CNR-DT200 (2006) Guide for the design and construction of externally bonded FRP systems for strengthening existing structures. C.N.R. National Reaserch Council, Italy
8. Sinha BP (1978) A simplified ultimate load analysis of laterally loaded model orthotropic brickwork panels of low tensile strength. J Struct Eng ASCE 56(4):81–84
9. Gazzola EA, Drysdale RG, Essawy AS (1985) Bending of concrete masonry walls at different angles to the bed joints. In: Proceedings of 3rd North. Amer. Mas. Conf., Arlington, Texas, USA, Paper 27
10. Cecchi A, Milani G, Tralli A (2007) A Reissner-Mindlin limit analysis model for out-of-plane loaded running bond masonry walls. Int J Solids Struct 44:1438–1460
11. Lourenço PB, de Borst R, Rots JG (1997) A plane stress softening plasticity model for orthotropic materials. Int J Numer Meth Eng 40:4033–4057
12. Milani G, Lourenço PB, Tralli A (2006) Homogenised limit analysis of masonry walls. Part II: structural examples. Comput Struct 84(3–4):181–195
13. Milani G, Lourenço PB, Tralli A (2006) Homogenization approach for the limit analysis of out-of-plane loaded masonry walls. J Struct Eng 132(10):1650–1663
14. de Buhan P, de Felice G (1997) A homogenisation approach to the ultimate strength of brick masonry. J Mech Phys Solids 45(7):1085–1104
15. Pietruszczak S, Ushaksaraei R (2003) Description of inelastic behaviour of structural masonry. Int J Solids Struct 40:4003–4019
16. Lotfi HR, Shing BP (1994) Interface model applied to fracture of masonry structures. J Struct Eng 120:63–80
17. Lourenço PB, Rots J (1997) A multi-surface interface model for the analysis of masonry structures. J Eng Mech 123(7):660–668
18. Lourenço PB (1997) An anisotropic macro-model for masonry plates and shells: implementation and validation. Report 03.21.1.3.07, University of Delft, Delft, Holland and University of Minho, Guimarães, Portugal
19. Lourenço PB, Rots JG, Blaauwendraad J (1998) Continuum model for masonry: parameter estimation and validation. J Struct Eng 124(6):642–652
20. Luciano R, Sacco E (1997) Homogenization technique and damage model for old masonry material. Int J Solids Struct 34(4):3191–3208
21. Cecchi A, Milani G (2008) A kinematic FE limit analysis model for thick English bond masonry walls. Int J Solids Struct 45:1302–1331
22. Mosallam AS (2007) Out-of-plane flexural behavior of unreinforced red brick walls strengthened with FRP composites. Compos Part B Eng 38(5–6):559–574
23. Chong VL, Southcombe C, May IM (1994) The behaviour of laterally loaded masonry panels with openings. In: Proceedings of 3rd Int. Masonry Conf. Proc. Brit. Mas. Soc. London, UK, 178–182
24. Suquet P (1983) Analyse limite et homogeneisation. Comptes Rendus de l'Academie des Sciences-Series IIB Mechanics 296: 1355–1358
25. Orduña A, Lourenço PB (2005) Three-dimensional limit analysis of rigid blocks assemblages. Part I: Torsion failure on frictional joints and limit analysis formulation. Int J Solids Struct 42(18–19): 5140–5160
26. Ferris M, Tin-Loi F (2001) Limit analysis of frictional block assemblies as a mathematical program with complementarity constraints. Int J Mech Sci 43:209–224
27. Begg D, Fishwick R (1995) Numerical analysis of rigid block structures including sliding. In: Middleton J, Pande G (eds) Computer Methods in Structural Masonry, vol 3, pp 177–183
28. Strand 7.2. User's Guide and Theoretical Manual
29. Krabbenhoft K, Lyamin AV, Hjiaj M, Sloan SW (2005) A new discontinuous upper bound limit analysis formulation. Int J Numer Methods Eng 63:1069–1088
30. D.M.LL.PP. (1987) Norme tecniche per la progettazione, esecuzione e collaudo degli edifici in muratura e per il loro consolidamento [Technical norms for the design, execution and test of masonry buildings and for their rehabilitation], Italian national norm
31. Sloan SW, Kleeman PW (1995) Upper bound limit analysis using discontinuous velocity fields. Comput Methods Appl Mech Eng 127(1–4):293–314
32. Makrodimopoulos A, Martin CM (2006) Lower bound limit analysis of cohesive-frictional materials using second-order cone programming. Int J Numer Methods Eng 66(4):604–634
33. Krabbenhoft K, Lyamin AV, Sloan SW (2007) Formulation and solution of some plasticity problems as conic programs. Int J Solids Struct 44:1533–1549
34. Krabbenhoft K, Lyamin AV, Sloan SW (2008) Three-dimensional Mohr-Coulomb plasticity using semidefinite programming. Commun Numer Methods Eng (in press)